JOURNAL OF PETROLOGY

Journal of Petrology, 2020, Vol. 61, No. 9: egaa067
doi: 10.1093/petrology/egaa067
Advance Access Publication Date: 18 June 2020
Original Article

OXFORD

A Disequilibrium Reactive Transport Model for Mantle Magmatism

Beñat Oliveira [1]*, Juan Carlos Afonso [1,2] and Romain Tilhac [1,3]

[1]ARC Centre of Excellence for Core to Crust Fluid Systems (CCFS) and GEMOC, Department of Earth and Planetary Sciences, Macquarie University, Sydney, NSW 2109, Australia; [2]Centre for Earth Evolution and Dynamics, Department of Geosciences, University of Oslo, 0371 Oslo, Norway; [3]Instituto Andaluz de Ciencias de la Tierra (IACT), CSIC–Universidad de Granada, 18100 Armilla, Granada, Spain

*Corresponding author. E-mail address: oliveira.bravo.b@gmail.com

Received 6 December 2018; Accepted 6 June 2020

ABSTRACT

Besides standard thermo-mechanical conservation laws, a general description of mantle magmatism requires the simultaneous consideration of phase changes (e.g. from solid to liquid), chemical reactions (i.e. exchange of chemical components) and multiple dynamic phases (e.g. liquid percolating through a deforming matrix). Typically, these processes evolve at different rates, over multiple spatial scales and exhibit complex feedback loops and disequilibrium features. Partially as a result of these complexities, integrated descriptions of the thermal, mechanical and chemical evolution of mantle magmatism have been challenging for numerical models. Here we present a conceptual and numerical model that provides a versatile platform to study the dynamics and nonlinear feedbacks inherent in mantle magmatism and to make quantitative comparisons between petrological and geochemical datasets. Our model is based on the combination of three main modules: (1) a Two-Phase, Multi-Component, Reactive Transport module that describes how liquids and solids evolve in space and time; (2) a melting formalism, called Dynamic Disequilibirum Melting, based on thermodynamic grounds and capable of describing the chemical exchange of major elements between phases in disequilibrium; (3) a grain-scale model for diffusion-controlled trace-element mass transfer. We illustrate some of the benefits of the model by analyzing both major and trace elements during mantle magmatism in a mid-ocean ridge-like context. We systematically explore the effects of mantle potential temperature, upwelling velocity, degree of equilibrium and hetererogeneous sources on the compositional variability of melts and residual peridotites. Our model not only reproduces the main thermo-chemical features of decompression melting but also predicts counter-intuitive differentiation trends as a consequence of phase changes and transport occurring in disequilibrium. These include a negative correlation between Na_2O and FeO in melts generated at the same T_p and the continued increase of the melt's CaO/Al_2O_3 after Cpx exhaustion. Our model results also emphasize the role of disequilibrium arising from diffusion for the interpretation of trace-element signatures. The latter is shown to be able to reconcile the major- and trace-element compositions of abyssal peridotites with field evidence indicating extensive reaction between peridotites and melts. The combination of chemical disequilibrium of major elements and sluggish diffusion of trace elements may also result in weakened middle rare earth to heavy rare earth depletion comparable with the effect of residual garnet in mid-ocean ridge basalt, despite its absence in the modelled melts source. We also find that the crystallization of basalts ascending in disequilibrium through the asthenospheric mantle could be responsible for the formation of olivine gabbros and wehrlites that are observed in the deep sections of ophiolites. The presented framework is general and readily extendable to accommodate additional processes of geological relevance (e.g. melting in the presence of volatiles and/or of complex heterogeneous sources, refertilization of the lithospheric mantle, magma channelization and shallow processes) and the implementation of other geochemical and isotopic proxies. Here

we illustrate the effect of heterogeneous sources on the thermo-mechanical-chemical evolution of melts and residues using a mixed peridotite–pyroxenite source.

Key words: thermodynamic modelling; kinetics; diffusion; magma genesis; heterogeneous melting

INTRODUCTION

Mantle magmatism is one of the main consequences of the thermal evolution and differentiation of the Earth and other terrestrial planets. It is the root cause behind some of the most important processes controlling the chemical evolution of the Earth and its atmosphere (e.g. planetary differentiation, mantle depletion and metasomatism, ore formation, crustal growth, volcanism, etc.). Given its impact on the bulk physical properties of the rocks, partial melting also exerts a strong influence on the mechanical behaviour of the mantle (e.g. focusing of deformation) and affects the interpretation of geophysical signatures (e.g. seismic velocities, electrical conductivity); yet mantle magmatism is a complex phenomenon governed by non-linear thermo-chemical-mechanical feedback loops at multiple scales. Modelling these complexities and their effects on observable geochemical and geophysical signatures remain challenging tasks.

Langmuir *et al.* (1992), Asimow (2001) and Brown & Lesher (2016), amongst others, have argued that any quantitative and predictive framework for mantle magmatism should be based on (1) a melting function, (2) a chemistry function and (3) a mixing function. The first two describe the amount of generated melt (i.e. melting function) and the actual chemical compositions of both the melt and the solid residue (i.e. chemistry function) as a function of pressure, temperature, and source composition. The role of the mixing function is to describe the spatial distribution of both solid and melt (i.e. solid flow field and melt mixing or extraction pathways) within the melting regime.

Melting and chemistry functions have traditionally been formulated in terms of end-member equilibrium models; namely, batch and fractional melting models (Gast, 1968; Shaw, 1970). The former implies that melts remain in equilibrium within their source at all times, whereas in the latter, melts are continuously extracted and isolated (only infinitesimal amounts of melt produced at each increment are assumed in equilibrium). Other models assume the presence of a critical melt fraction in equilibrium with the source prior to extraction, as in near-fractional models (e.g. Johnson *et al.*, 1990; Kinzler & Grove, 1992). Despite their usefulness and popularity, these approaches have two important drawbacks. First, the equilibrium assumption may not hold in cases where diffusion rates within mineral grains are too slow to allow for complete equilibration between melt and residue (e.g. Van Orman *et al.*, 2002*a*). Second, the (thermo)dynamic nature of melting and melt migration is neglected (i.e. these approaches refer to static, atemporal melt extraction mechanisms).

As for the mixing function, the geodynamic community has provided the groundwork for the modelling of mantle magmatism via two-phase formulations (McKenzie, 1984; Richter & McKenzie, 1984; Spiegelman, 1993; Bercovici *et al.*, 2001; Spiegelman *et al.*, 2001; Bercovici & Ricard, 2003). However, the main goal of these studies has been to understand the dynamic evolution of melt and solid mantle; the joint treatment of the (highly coupled) chemical and mechanical evolution of the two-phase system is less well developed.

From a geological perspective, however, there is clear evidence that melts and peridotites interact thermally, mechanically and chemically—which means that despite being constructed independently, the mixing function cannot be separated from the chemistry and melting functions. For instance, the existence of replacive dunite and harzburgite channels in ophiolites indicates that extensive reactions must occur between migrating melts and host peridotites (e.g. Kelemen *et al.*, 1992; Braun & Kelemen, 2002; Abily & Ceuleneer, 2013; Dygert *et al.*, 2016). In contrast, there is experimental and theoretical evidence suggesting that low-volume melts (i.e. $<1\%$) can be interconnected (Waff & Bulau, 1979; von Bargen & Waff, 1986; Riley & Kohlstedt, 1991) and efficiently extracted from the melting regime (McKenzie, 1984; Richter & McKenzie, 1984; Spiegelman & McKenzie, 1987). This points towards significant disequilibrium arising from rapid melt extraction and migration (Faul, 2001; Connolly *et al.*, 2009), in agreement with U-series disequilibria measured in mid-ocean ridge basalts (MORB) (e.g. McKenzie, 1985; Lundstrom, 2003; Van Orman *et al.*, 2006).

Recent models of two-phase reactive transport aim at providing an integrated approach to study the main thermo-chemical feedbacks thought to dominate mantle magmatism (Šrámek *et al.*, 2007; Katz, 2008; Tirone *et al.*, 2009; Rudge *et al.*, 2011; Keller & Katz, 2016; Oliveira *et al.*, 2018; Tirone & Sessing, 2017). The core of these models resides in the coupling of a petrological model (i.e. joint melting and chemical functions) with a multi-phase reactive transport formalism (i.e. mixing function). As such, dynamically evolving chemical compositions retrieved from these models are the result of the integrated reaction and transport rates (i.e. processes) that any given solid or melt parcel experiences along its trajectory through space and time (P–T–t path). Whereas the transport formalism is relatively similar between authors, the petrological description of the system differs significantly. Except for a few kinetic

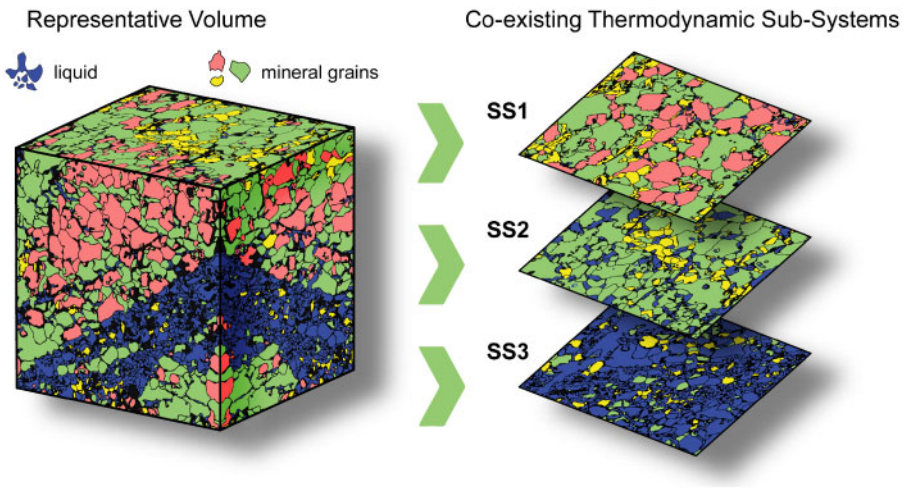

Fig. 1. Illustration of the three thermodynamic subsystems coexisting within a representative volume. The latter is composed of a solid made up of several mineral grains (green, pink and yellow) and a liquid phase (in blue). At a local scale, phases occupy a finite space, and they interact across well-defined boundaries (left panel). The spatial distribution of phases within the representative volume is lost when the three subsystems are defined at the system scale (right panel). Physical properties and phase abundances of solid and liquid phases within each of the three subsystems are considered average quantities over the entire representative volume. The first subsystem (ss1) is made up of the isolated solid; subsystem two (ss2) consists of the portions of solid and liquid allowed to re-equilibrate with each other; and the third subsystem (ss3) refers to the isolated liquid phase. The scale of the representative volume chosen for illustration is not exclusive and applications from microstructural to regional scales can be envisaged, depending on the time frame considered. Image is a modified thin section courtesy of H. Henry.

formulations based on non-equilibrium thermodynamic grounds (e.g. Šrámek *et al.*, 2007; Rudge *et al.*, 2011), most approaches to date rely on local thermodynamic equilibrium principles (see De Groot & Mazur, 2013). These range from empirical phase-equilibria parameterizations (e.g. Katz, 2008; Keller & Katz, 2016) to thermodynamically constrained models based on Gibbs free-energy minimizations (Asimow, 2002; Tirone *et al.*, 2009; Oliveira *et al.*, 2018; Tirone & Sessing, 2017). Furthermore, the majority of these models focus on the large-scale, average properties of the system by making use of macro-scale averaging postulates (Keller & Suckale, 2019). This renders them poorly suited for studying the nature of small-scale processes affecting mantle magmatism (e.g. microstructural evolution, diffusional re-equilibration of major and trace elements, isotopic fractionation) and their effects on the average properties of the large-scale system.

This paper represents an initial effort to formulate a general quantitative framework for studying the main petrological, geochemical, and dynamic consequences of multi-phase disequilibrium reactive transport for mantle magmatism. Our model combines three main components: (1) a Two-Phase, Multi-Component, Reactive Transport (TPMCRT) module that provides a numerical solution to the governing conservation equations (Oliveira *et al.*, 2018); (2) a Dynamic Disequilibirum Melting (DDM) model for the joint treatment of the melting, chemistry and mixing functions; (3) a grain-scale model for diffusion-controlled trace-element mass transfer.

Our DDM model makes use of internally consistent thermodynamic models and databases (see also Asimow, 2001; Tirone, 2018) and allows us to simulate different degrees of equilibrium between accumulated melts and residual solids. This is achieved by defining three independent thermodynamic subsystems within a given representative volume (Fig. 1). Briefly, the first subsystem (ss1) refers to that portion of solid that remains chemically isolated from any other subsystem. The second subsystem (ss2) is made up of those volumes of both solid and melt that can exchange mass and equilibrate with each other. The third subsystem (ss3) represents the accumulated melt fraction. Each subsystem is in disequilibrium with each other, but equilibrium principles are applied locally within subsystems (i.e. independent Gibbs free-energy minimizations are run based on subsystem pressure, temperature and bulk composition conditions). Therefore, in contrast to other melting models, our DDM model can explicitly track the evolution of different lithologies in every subsystem (see details in the section 'Dynamic Disequilibrium Melting model').

Because trace elements have insignificant effects on the stability of the phase assemblage, we propose a separate (uncoupled) granular-scale model for trace element transport. As in previous studies (Qin, 1992; Iwamori, 1993; Van Orman *et al.*, 2002*a*), trace-element exchange between mineral grains and melt is controlled by diffusional re-equilibration and phase changes. Unlike previous studies, however, mineral proportions are retrieved in a thermodynamically consistent manner from the DDM model as functions of temperature, pressure and bulk composition. Because of the sensitivity of trace-element fractionation to changes in pressure, temperature and chemical

composition during different magmatic processes (e.g. exhaustion of clinopyroxene during partial melting), and extensive experimental data available in the literature (for rare earth elements in particular), the diffusion-controlled disequilibrium trace-element model is a key component for an integrated interpretation of geochemical processes and isotopic signatures related to mantle magmatism.

The remainder of this paper is organized as follows. In the next section we briefly review the local thermodynamic equilibrium hypothesis in the context of this work. The general methods and main components of our model are described in 'General methods'. Numerical results of one-dimensional decompression melting experiments are presented in 'Numerical examples', which showcases the benefits of our integrated approach when exploring the compositional variability of modelled melts and peridotites in the context of mid-ocean ridges. A discussion on geochemical implications and model limitations is provided in the 'Discussion' section, followed by concluding remarks in 'Conclusions'.

BACKGROUND

Local thermodynamic equilibrium is the main assumption made throughout this study. For the sake of clarity, we briefly review its meaning and discuss its implications for the dynamically evolving systems addressed in this study.

The so-called local equilibrium hypothesis is the fundamental assumption behind the classical theory of irreversible thermodynamics, also known as Classical Irreversible Thermodynamics (CIT) (see Lebon *et al.*, 2008). It states that even in systems out of (global) equilibrium, all thermodynamic relations defined at equilibrium can still be used, but only locally and instantaneously. It therefore assigns an explicit space and time dependence to all thermodynamic quantities of interest (e.g. entropy, chemical potential). Conceptually, the global system is split into 'local' subsystems or cells that are large enough for microscopic fluctuations to be negligible (i.e. thermodynamic equilibrium is locally realized) but sufficiently small compared with the distances over which the main field variables vary. In the context of dynamically evolving systems, transport rates (e.g. melt migration) may introduce gradients in thermodynamic potentials (e.g. chemical potential) and field variables (e.g. temperature), both globally and locally. Thermodynamics dictates that the presence of gradients in thermodynamic potentials will drive reactions (i.e. chemical, thermal and mechanical) towards equilibrium. In reality, complete re-equilibration may or may not materialize depending on the relative rates at which transport and chemical reactions occur. For instance, fast kinetics will tend to equilibrate the system regardless of how fast mass and energy evolve. In contrast, slow kinetics (e.g. sluggish diffusion) and fast transport processes (e.g. melt channeling) will promote disequilibrium.

In summary, local thermodynamic equilibrium in dynamically evolving systems is achieved when rates of equilibrating reactions are locally much faster than the rates of 'disequilibrating' transport processes. However, the spatial and temporal scales at which equilibrium principles apply depend on the problem under consideration (e.g. reaction kinetics, diffusion), and as such, need to be carefully defined.

Analogous to the local thermodynamic equilibrium hypothesis, in this study we split the dynamically evolving system into representative volumes where separate thermodynamic subsystems are assumed to coexist (Fig. 1). By 'thermodynamic subsystem' we imply an aggregate of thermodynamic phases (i.e. mineral grains) where local thermodynamic equilibrium principles apply, whereas 'representative volume' refers to the minimum spatial domain that includes a representative sample of all small-scale heterogeneities (e.g. grains, voids, melt inclusions). As stated above, the three subsystems within a representative volume may not be in equilibrium with each other. Both DDM and TPMCRT models operate at the representative volume scale, and thus small-scale properties are replaced by set of continuum (and averaged) fields.

GENERAL METHODS

Dynamic Disequilibrium Melting model

The general idea behind the DDM model is summarized in Figs 1 and 2. To guide the reader through the model description, we describe it below as a sequence of four steps (Fig. 2).

Let us consider a starting representative volume made up of a solid (*s*), which is composed of several thermodynamic phases or mineral grains (*tp*), and one liquid (*l*) phase (Fig. 1; the phases within the representative volume in Fig. 1 have been rearranged in Fig. 2, step 1). Within this representative volume, we identify up to three independent thermodynamic subsystems (Fig. 2, step 2), which will be allowed to follow different equilibration paths. The first subsystem (ss1) represents the portion of the starting solid that will be kept isolated from any mass transfer with other adjacent subsystems. An analogy in a real scenario could be the unmetasomatized peridotite away from high-porosity channels (where melt percolates preferentially and reacts with the solid matrix). The second subsystem (ss2) is made up of those volumes of solid and liquid that will be allowed to exchange mass and equilibrate (react) with each other during a time interval; in other words, the volumes of peridotites and melts undergoing phase transformation (e.g. melting, crystallization) in equilibrium with each other, as it could happen within a reaction rim surrounding a melt channel. The bulk composition of this second subsystem will be a weighted average of both the liquid and the solid

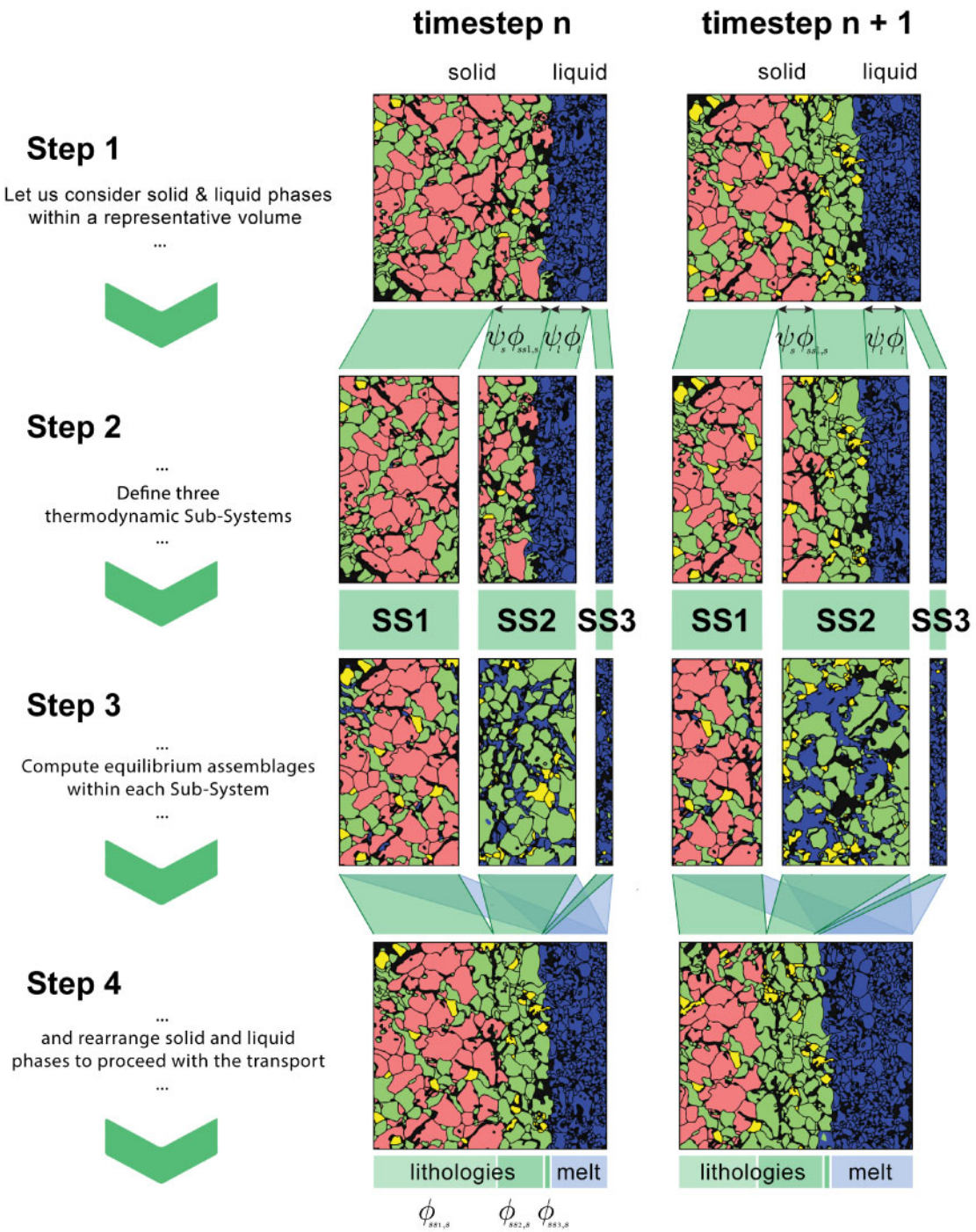

Fig. 2. Four main steps of the Dynamic Disequilibrium Melting (DDM) model for two consecutive time steps. First, solid and liquid phases are identified within representative volumes. Second, three thermodynamic subsystems are defined: ss1 is isolated solid; ss2 is a mixture of solid and liquid phases that are allowed to equilibrate with each other (their relative proportions being defined with $\psi_s\phi_{ss1,s}$ and $\psi_l\phi_l$); ss3 is isolated liquid. Within these subsystems the new equilibrium assemblages (for the current time step) are computed via free-energy minimization for its local P–T–c^b conditions (step three). In general, phase transformation in each subsystem will lead to melting and/or crystallization of new mineral phases. The fourth step consists on rearranging these newly formed thermodynamic phases into solid and liquid dynamic phases to proceed with the transport computations (TPMCRT model). We keep track of the different solid lithologies (solid phases formed in equilibrium within each of the subsystems), whereas liquids are assumed to form a single locally uniform melt. It should be noted that the solid keeps its heterogeneity during transport (from time step n to time step $n + 1$), and that the extent of equilibration in the solid is computed within the isolated solid phase only (i.e. $\psi_s\phi_{ss1,s}$, step 2), as the other solid lithologies are considered to always equilibrate within ss2.

fractions, and the partitioning of chemical components between the different thermodynamic phases will be computed assuming local equilibrium. The third subsystem (ss3) represents isolated melts not reacting with other adjacent subsystems. In this case, an analogy could be the interior of melt channels or dikes.

As pointed out in the 'Background' section, the extent of equilibration between the migrating liquid and the surrounding solid depends on the kinetics of the reactions and the residence time. Therefore, the actual number (and type) of subsystems will vary between one and three depending on the local conditions. To this end, we represent the extent of equilibration with two coefficients ψ_s and ψ_l, one for each phase (Fig. 2, step 2). These coefficients range from zero (i.e. no equilibration) to unity (i.e. fully equilibrated; subsystems ss1 and/or ss3 are absent). Further details on the nature of ψ are given in 'Extent of equilibration of solid and liquid phases, crystallization and other melting models'.

Once the subsystems are conceptually defined, we can proceed with separate thermodynamic computations (i.e. Gibbs free-energy minimization) based on their local pressure, temperature and bulk compositions. In this third step (Fig. 2, step 3), there is no mass or energy transfer between subsystems (i.e. closed systems). However, new solid and liquid fractions can be formed within each of these subsystems (Fig. 2, step 3). For instance, solidification can occur in the isolated melt subsystem (Fig. 2, step 3, ss3) and/or new melt can be created in any of the solid subsystems depending on their P–T paths (Fig. 2, step 3, ss1 and ss2). Details on the thermodynamic computations are provided in sections 'Local P–T–c^b conditions' and 'Thermodynamic model'.

The last step consists of rearranging the different solid and liquid phases so that both the DDM model and the TPMCRT problem are made compatible (Fig. 2, step 4). From a chemical point of view, the melts are considered to form a single and uniform phase (pooled, equilibrated melt), whereas the three solid subsystems (ss1 and the solids within ss2 and ss3) retain their individual compositions (and their properties) and therefore represent distinct lithologies (Fig. 2, step 4). In this way, we keep track of individual chemical compositions recorded within the isolated solid, within the equilibrated subsystem, and in the newly crystallized minerals within the isolated liquid parcel. From a dynamic point of view, however, all three solids are transported by a unique (solid) velocity field (see the section 'Two-phase multi-component reactive transport model'). This means that we cannot model explicitly particulate transport inside the liquid in the current formulation (e.g. xenocrysts being transported by the melt).

Extent of equilibration of solid and liquid phases, crystallization and other melting models

The extent of chemical, mechanical and thermal equilibrium between solid and liquid phases depends upon the rates of equilibrating reactions versus the rates of 'disequilibrating' transport processes. These rates in turn will vary according to the specific kinetics of the considered reactions, diffusivities, the state of stress, and the grain size, among other second-order factors. For the purposes of this study, we assume thermal equilibrium at the scale of the representative volume, implying that transport processes are sufficiently slow for the temperature to equilibrate locally between phases. In the context of melt generation and migration via porous flow, this assumption is reasonable (e.g. Iwamori *et al.*, 1995). We refer the reader to Schmeling *et al.* (2017) for a discussion on the validity of this assumption and other alternatives.

Because reactions are diffusion-limited (scales as length squared per time) and transport is often advective (scales as length per time), it is desirable to approximate the extent of equilibrium with a characteristic length scale of diffusion (L_D)

$$L_D = 2\sqrt{D^*\tau^*} \tag{1}$$

where D^* refers to a characteristic diffusion coefficient and τ^* is a characteristic time scale of residence. Defining a single D^* for a given representative volume is challenging, as diffusion coefficients are known to vary significantly between mineral phases as well as with pressure, temperature and chemical composition (e.g. Chakraborty & Ganguly, 1992; Ganguly *et al.*, 1998). Furthermore, chemical diffusion is, in general, much faster in liquids than in solid phases. We approximate the re-equilibration behavior within a representative volume by defining two parameters (one for the solid phase, ψ_s, and the other for the liquid, ψ_l) representing different extents of equilibration. More precisely, they represent the portion of either isolated solid or liquid allowed to equilibrate (Fig. 2)

$$\psi_{s,l} = \begin{cases} L_D^{s,l}/L_{s,l} & L_D^{s,l} < L_{s,l} \\ 1 & L_D^{s,l} \geq L_{s,l} \end{cases} \tag{2}$$

where $L_{s,l}$ in this case refers to the length of solid or liquid phase (e.g. mean grain size).

According to equation (2), ψ_s and ψ_l range from zero to unity: from complete disequilibrium owing to slow diffusion and/or short residence time to complete as a consequence of fast diffusion and/or long residence time. According to equation (1), it would take ~2 Myr to equilibrate a 5 mm solid grain if $= 10^{-15}\,\mathrm{cm^2\,s^{-1}}$ (i.e. $\tau^* = L_D^2/4/ \approx 2$ Myr and $\psi_s = 1{\cdot}2649 \times 10^{-7}\sqrt{\tau^*}$), whereas equilibrium would be achieved in only 2 kyr with $D^* = 10^{-12}\,\mathrm{cm^2\,s^{-1}}$ ($\psi_s = 4 \times 10^{-6}\sqrt{\tau^*}$).

Similar models exist in the literature (e.g. Asimow, 2001; Tirone & Sessing, 2017; Tirone, 2018). However, to the best of our knowledge, the DDM model presented here is the only one that explicitly takes an out-of-equilibrium liquid phase into account. In other words, our model allows crystallization of isolated solids within the liquid phase. For most melting scenarios, where liquids are considered to equilibrate instantaneously (i.e. $\psi_l = 1$), ss3 does not exist. However, this third subsystem is necessary to study fast disequilibrium crystallization processes (e.g. fractional crystallization) that may occur within high flux melt conduits or in magma

chambers (e.g. Langmuir *et al.*, 1992). Our melting model is, therefore, truly frame-invariant and equally valid as a 'crystallizing' model.

The DDM model encompasses and generalizes traditional batch/equilibrium and fractional melting/crystallization models for dynamically evolving systems. Following previous studies (e.g. Tirone, 2018), we define two end-member melting models: (1) Dynamic Equilibrium Melting model (DEM; $\psi_s = 1$ and $\psi_l = 1$) and (2) Dynamic Fractional Melting model (DFM; $\psi_s = 0$ and $\psi_l = 1$).

Local P–T–c^b *conditions*

Pressure P, temperature T, and bulk composition c^b are sufficient to define the thermodynamic state of every subsystem in our model. Because the DDM model considers up to three subsystems in local equilibrium, three distinct sets of P–T–c^b conditions need to be defined, one for each subsystem.

Given the assumption of thermal equilibrium within each representative volume (see section 'Extent of equilibration of solid and liquid phases, crystallization and other melting models'), temperature is the same across its subsystems. As mentioned above, however, pressure and bulk compositions differ between subsystems. Pressures and chemical compositions for ss1 (e.g. P_s and $c^b_{ss1,s}$) and ss3 (e.g. P_f and c^b_f) are obtained directly from the TPMCRT model, the details of which are shown below. Because subsystem ss2 consists of the portions of solid and liquid allowed to re-equilibrate with each other, the bulk composition of ss2, c^b_{ss2}, is a weighted average of its constituents

$$c^b_{ss2} = \frac{100(\psi_s\phi_{ss1,s}\rho_{ss1,s}c^b_{ss1,s} + \phi_{ss2,s}\rho_{ss2,s}c^b_{ss2,s} + \phi_{ss3,s}\rho_{ss3,s}c^b_{ss3,s} + \psi_l\phi_l\rho_l c^b_l}{\psi_s\phi_{ss1,s}\rho_{ss1,s} + \phi_{ss2,s}\rho_{ss2,s} + \phi_{ss3,s}\rho_{ss3,s} + \psi_l\phi_l\rho_l} \tag{3}$$

where bulk composition is expressed in terms of wt% of chemical component b (i.e. SiO_2, MgO, FeO, etc.). $\phi_{*,s}$ is the volume fraction of a given solid phase within a given subsystem (*; ss1, ss2 or ss3) with respect to the total volume of the representative volume. $\rho_{*,s}$ refers to their respective densities. ϕ_l and ρ_l are the liquid's volume fraction and densities, respectively. $\psi_s\phi_{ss1,s}$ and $\psi_l\phi_l$ refer to the fractions of isolated solid and liquid allowed to equilibrate within ss2, respectively (see Fig. 2).

As for pressure P_{ss2}, we assume that the pressure of the reacting mixture is the same as that of the liquid pressure for all the components within ss2, and thus $P_{ss2} = P_l$.

Thermodynamic model

Energy minimization in all subsystems is done with components of the software Perple_X (Connolly *et al.*, 2009) and the thermodynamic model of Jennings & Holland (2015). This allows us to retrieve local equilibrium mineral assemblages (i.e. thermodynamic phase abundances and their compositions), their relevant physical properties (e.g. density, seismic velocities, heat capacities), and closure terms (e.g. mass-transfer rates, heat absorption or release owing to phase change) everywhere in the system.

Two-phase multi-component reactive transport model

Any Two-Phase Multi-Component Reactive Transport model needs to be grounded on mass, momentum and energy conservation equations. Although the full derivation of these equations can be found elsewhere (e.g. McKenzie, 1984; Bercovici *et al.*, 2001; Šrámek *et al.*, 2007; Katz, 2008; Rudge *et al.*, 2011; Keller & Katz, 2016; Oliveira *et al.*, 2018; Keller & Suckale, 2019), we briefly summarize them here for completeness. The coupling between these standard equations and the DDM model is addressed in 'Coupling between the DDM and the TPMCRT models: Tracking lithologies, Closure terms and Thermodynamic properties'. Table 1 includes all the variables appearing in the formulation.

Mass conservation

Neglecting bulk mass diffusion, mass conservation in the solid (s) and liquid (l) phases is controlled by

$$\frac{\partial\phi_s\rho_s}{\partial t} + \nabla\cdot(\phi_s\rho_s v_s) = -\Gamma \tag{4}$$

$$\frac{\partial\phi_l\rho_l}{\partial t} + \nabla\cdot(\phi\rho_l v_l) = \Gamma \tag{5}$$

where Γ is the rate of mass exchange (or simply, melting rate) and v is the velocity. Solid and liquid masses are expressed in terms of their volume fractions, ϕ, and densities, ρ, and evolve owing to advection, compaction and phase change. When a solid parcel undergoes melting, its mass should locally decrease and cause a local increase in the liquid's mass (i.e. positive Γ). Because of mass-balance constraints, volume fractions obey $\phi_s + \phi_l = 1$.

In addition, solid and liquid phases making up the system are composed of basic chemical components (i.e. SiO_2, MgO, FeO, etc.). Mass conservation of basic chemical component b for both dynamic phases is given by

$$\frac{\partial\phi_s\rho_s c^b_s}{\partial t} + \nabla\cdot(\phi_s\rho_s c^b_s v_s) = -\Gamma^b \tag{6}$$

$$\frac{\partial\phi_l\rho_l c^b_l}{\partial t} + \nabla\cdot(\phi\rho_l c^b_l v_l) = \Gamma^b \tag{7}$$

where c^b_s and c^b_l are the concentrations, in wt%, of basic component b in the solid and liquid phases, respectively, for a given representative volume (e.g. $c_l^{SiO_2}$ refers to the concentration of SiO_2 inside the liquid phase). Γ^b is the rate of chemical exchange of basic component b between the two dynamic phases. Concentrations of major elements are required to sum to unity as $\sum_b c^b_s = \sum_b c^b_l = 1$, and therefore $\sum_b \Gamma^b = \Gamma$.

Table 1: Nomenclature and reference values

Variable	Description	Unit	Value
α	Thermal expansion	K^{-1}	
c	Composition	none	
c_p	Heat capacity	$J\,kg^{-1}\,K^{-1}$	
d	Mechanical interaction coefficient	$Pa\,s\,m^{-2}$	$\mu_l\phi^2/k(\phi)$
ρ	Density	$kg\,m^{-3}$	
D	Diffusion coefficient	$m^2\,s^{-1}$	
ΔH	Enthalpy difference	$J\,kg^{-1}$	
g	Gravity	$m\,s^{-2}$	9·81
K	Partition coefficient	none	
n_{tp}	Number of grains of a given thermodynamic phase (per unit of volume)	m^{-3}	
M	Interface momentum-transfer rate	$Pa\,m^{-1}$	$d(v_l - v_s) - P_i\nabla\phi_l$
$K(\phi)$	Kozeny–Carman type permeability function	m^2	$k_0\phi^n$
K_0	Permeability constant	m^2	10^{-6}
n	Permeability exponent	none	2
k_T	Thermal conductivity	$W\,m^{-1}\,K^{-1}$	
P	Pressure	Pa	
ΔP	Pressure difference	Pa	
P_0	Pressure at the deep solidus	Pa	
$\boldsymbol{q}$	Diffusive heat flux	$J\,m^{-2}\,s^{-1}$	
R_{tp}	Radii of mineral grain	m	$\sqrt[3]{\frac{\phi_{tp}}{4/3\pi n_{tp}}}$
R	Universal gas constant	$J\,mol^{-1}\,K^{-1}$	8·3144598
τ	Deviatoric stress	Pa	$\mu\left[\nabla v + [\nabla v]' - \frac{2}{3}(\nabla\cdot v)\boldsymbol{I}\right]$
T	Temperature	°C	
$\boldsymbol{v}$	Velocity	$m\,s^{-1}$	
$\Delta\boldsymbol{v}$	Velocity difference	$m\,s^{-1}$	$(v_s - v_l)$
μ_{max}	Maximum viscosity	Pa s	10^{24}
μ_s^{diff}	Diffusion-creep viscosity	Pa s	$A\exp\left(\frac{R+PV}{RT}\right)$
μ	Shear viscosity	Pa s	$\left(\frac{1}{\mu_s^{diff}} + \frac{1}{\mu_{max}}\right)^{-1}$
Γ	Solid-to-liquid mass-transfer rate	$kg\,m^{-3}\,s^{-1}$	
ϕ	Melt volume fraction (porosity)	none	
Φ	Any general property		
ψ	Re-equilibration parameter	none	
Ψ	Rate of work against deformation	$J\,m^{-3}\,s^{-1}$	
Index		Index	
s, l	Solid, liquid	*b, e*	Basic and trace-element component
tp	Thermodynamic phase or mineral	ss1, ss2, ss3	Subsystem 1, 2 and 3

It is often desirable to track mass changes in all subsystems along their respective paths. Using Lagrangian derivatives, the previous equations can be rewritten as

$$\frac{D_s\phi_s\rho_s}{Dt} = -\Gamma - \phi_s\rho_s\nabla\cdot v_s \tag{8}$$

$$\frac{D_l\phi_l\rho_l}{Dt} = \Gamma - \phi_l\rho_l\nabla\cdot v_l \tag{9}$$

$$\phi_s\rho_s\frac{D_s c_s^b}{Dt} = -\Gamma^b + c_s^b\Gamma \tag{10}$$

$$\phi_l\rho_l\frac{D_l c_l^b}{Dt} = \Gamma^b - c_l^b\Gamma \tag{11}$$

where $D_{s,l}/Dt = \partial(\,)/\partial t = v_{s,l}\cdot\nabla(\,)$ is the Lagrangian derivative, which advects phase fractions and concentrations with their corresponding velocities.

Mechanical problem

Neglecting inertia terms, the equations for conservation of momentum of the solid and liquid phases read

$$-\nabla\cdot(\phi_s\boldsymbol{\sigma}_s) = \phi_s\rho_s g + M \tag{12}$$

$$-\nabla\cdot(\phi_l\boldsymbol{\sigma}_l) = \phi_l\rho_l g - M \tag{13}$$

where M is the so-called interface force term per unit volume (see Bercovici *et al.*, 2001), g is the gravity vector, and $\boldsymbol{\sigma}_s$ and $\boldsymbol{\sigma}_l$ are the solid and liquid stress tensors, respectively. Both stress tensors can be split into volumetric and deviatoric parts as (now dropping subindices) $\boldsymbol{\sigma} = -P\cdot\boldsymbol{I} + \tau$, where $\boldsymbol{I}$ is the identity matrix, $P = -tr(\boldsymbol{\sigma})/3$ is the pressure, and τ is the traceless deviatoric stress tensor, $\tau = \mu(\nabla v + [\nabla v]^T - 2/3(\nabla\cdot v)\boldsymbol{I})$, where μ is the viscosity.

The interface force term (M) is a central ingredient of multi-phase formulations [see discussion by Oliveira *et al.* (2018)]. Within the geodynamic community, it is commonly modelled via phenomenological laws in terms of the velocity difference between the solid and liquid phases and the interfacial pressure (e.g. Bercovici *et al.*, 2001; Rudge *et al.*, 2011) as

$$M = d(v_l - v_s) - P_i\nabla\phi_l \tag{14}$$

where d is a symmetric, rheology-dependent, interaction coefficient (see Table 1 and 'Model Setup' for a

particular choice of d) and P_i is the interfacial pressure. The latter is assumed to be that of the liquid [see Bercovici & Ricard (2003), Oliveira *et al.* (2018), and in particular Keller & Suckale (2019), for further discussion regarding interfacial pressure]. In equation (14), surface tension and phase change effects on the momentum exchange between phases have been neglected (see e.g. Oliveira *et al.*, 2018, for a justification).

We close the mechanical problem with two additional relations: (1) the total mass conservation equation [obtained as the sum of equations (4) and (5)], and (2) a phenomenological law for the pressure difference between the two dynamic phases

$$\frac{\partial \overline{\rho}}{\partial t} + \nabla \cdot \overline{\rho \boldsymbol{v}} = 0 \tag{15}$$

$$\Delta P = -K_0 \frac{\mu_l + \mu_s}{\phi_l} (\nabla \cdot \boldsymbol{v}_S) \tag{16}$$

where $\overline{(\,)} = \phi_l (\,)_l + \phi_s (\,)_s$, $\Delta(\,) = (\,)_s - (\,)_l$ and K_0 is a dimensionless constant to account for grain/pore geometry. Equation (16) controls the pressure drop between phases owing to deformation of the solid matrix (via the divergence term; Šrámek *et al.*, 2007). The ratio $(\mu_l + \mu_s)/\phi_l$ can be interpreted as an effective volumetric viscosity for the two-phase mixture, making this formulation compatible with previous studies based on effective bulk viscosities (see McKenzie, 1984; Katz, 2008). We refer the reader to Keller & Suckale (2019) for further discussion on phenomenological laws for multi-phase formulations.

Energy problem

For simplicity, conservation of energy is formulated in terms of temperature. As stated above, we assume that the liquid moves sufficiently slowly through the porous matrix to allow complete thermal equilibration of the aggregate at a given spatio-temporal scale. With these assumptions, the temperature evolution equation reads

$$\overline{\rho c_p} \frac{\mathrm{D}_T T}{\mathrm{D}t} = Q - \nabla \cdot q + Q_{ad} + \Psi + \Delta H \Gamma \tag{17}$$

$\mathrm{D}_T(\,)T/\mathrm{D}t = \partial(\,)/\partial t + \boldsymbol{v}_T \nabla(\,)$ is the material derivative for temperature advection where $\boldsymbol{v}_T = 1/\overline{\rho c_p}(\phi_l \rho_l c_{p_l} \boldsymbol{v}_l + \phi_s \rho_s c_{p_s} \boldsymbol{v}_s)$. Internal heat sources are accounted for by the scalar term Q, and heat conduction by $\nabla \cdot q$. The term Q_{ad} represents the adiabatic effect [approximated as $Q_{ad} = T\overline{\alpha\rho} v_T^z g$, where α is the coefficient of thermal expansion and v_T^z is the vertical component of the velocity (Afonso & Zlotnik, 2011)], whereas $\Delta H\Gamma$ is the rate of heat released or absorbed by phase changes. The rate of work against deformation is computed as $\Psi = d\Delta \boldsymbol{v} \cdot \Delta \boldsymbol{v} + \phi_l \boldsymbol{\tau}_l : \nabla \boldsymbol{v} + \phi_s \boldsymbol{\tau}_s : \nabla \boldsymbol{v}_s + \frac{\mathrm{D}_s \phi_l}{\mathrm{D}t}$, composed of segregation, shear, and compaction flow dissipation terms.

Coupling between the DDM and the TPMCRT models: tracking lithologies, closure terms and thermodynamic ppproperties

The TPMCRT model provides the description of local solid and liquid P–T–c^b conditions, and their volume fractions ϕ_s and ϕ_l. The DDM model, however, requires tracking of volume fractions and chemical compositions for different lithologies (i.e. $\phi_{ss1,s}$, $\phi_{ss2,s}$, $\phi_{ss3,s}$, $c^b_{ss1,s}$, $c^b_{ss2,s}$, $c^b_{ss3,s}$). To satisfy mass conservation of different lithologies, six additional independent equations are needed for the six independent unknowns.

We circumvent this problem by modifying the traditional solid mass-conservation equations [equations (8) and (10)] to track the three lithologies separately as

$$\frac{\mathrm{D}_s \phi_{*,s} \rho_{*,s}}{\mathrm{D}t} = -\Gamma_{*,s} + \phi_{*,s} \rho_{*,s} \nabla \cdot \boldsymbol{v}_s \tag{18}$$

$$\phi_{*,s} \rho_{*,s} \frac{\mathrm{D}_s c^b_{*,s}}{\mathrm{D}t} = -\Gamma^b_{*,s} + c^b_{*,s} \Gamma^m_{*,s} \tag{19}$$

where subindex $*,s$ refers to any of the tracked solid lithologies. Again, because of mass-balance constraints, $\phi_s = \phi_{ss1,s} + \phi_{ss2,s} + \phi_{ss3,s}$, $\phi_s \rho_s = \phi_{ss1,s}\rho_{ss1,s} + \phi_{ss2,s}\rho_{ss2,s} + \phi_{ss3,s}\rho_{ss3,s}$, and thus $\Gamma = -\Gamma_{ss1,s} - \Gamma_{ss2,s} - \Gamma_{ss3,s}$. Chemical concentrations are required to sum to unity as $\sum_b c^b_{ss1,s} = \sum_b c^b_{ss2,s} = \sum_b c^b_{ss3,s} = 1$, and therefore $\Gamma^b = -\Gamma^b_{ss1,s} - \Gamma^b_{ss2,s} - \Gamma^b_{ss3,s}$ and consequently $\sum_b \Gamma^b = -\sum_b (\Gamma^b_{ss1,s} + \Gamma^b_{ss2,s} + \Gamma^b_{ss3,s}) = \Gamma$.

Equations (18), (19), (11), (12), (13), (15), (16) and (17) represent a linearly independent set of 12 equations for the same number of unknowns (i.e. $\phi_{ss1,s}$, $\phi_{ss2,s}$, $\phi_{ss3,s}$, c^b_f, $c^b_{ss1,s}$, $c^b_{ss2,s}$, $c^b_{ss3,s}$, P_f, P_s, v_f, v_s and T). This system of equations is solvable provided that the required material parameters (e.g. ρ_s, ρ_l, μ_s) and closure terms (i.e. mass-transfer rates, Γ, Γ^b) are known. The latter and some of the material parameters are retrieved from the thermodynamic model. For instance, the mass-transfer rate between solid and liquid phases, Γ, is obtained by adding differences in mass in the liquid phase (i.e. $\phi_l \rho_l$) before and after performing the free-energy minimization in each of the thermodynamic subsystems (for a given timescale). The same strategy is followed to compute the 'chemical mass'-transfer rate, Γ^b. The thermodynamic model also provides the absorbed or released heat owing to phase transformations. In detail, $\Delta H\Gamma$ is the sum of the absorbed or released latent heat resulting from phase changes within each subsystem, computed by multiplying the local specific enthalpy difference and the melting rate. Thermodynamic properties retrieved from the thermodynamic model include densities and heat capacities (or the abovementioned specific enthalpies) for all thermodynamic phases in equilibrium. Other material properties require additional constitutive laws (e.g. d, μ_s, μ_l, q). Because these are typically problem-dependent, we justify their particular choice in 'Model Setup'.

Specific details on the numerical coupling between the melting model and the reactive transport models are provided in Appendix A (this appendix also provides information regarding the diffusion-controlled trace-element model, which is presented below).

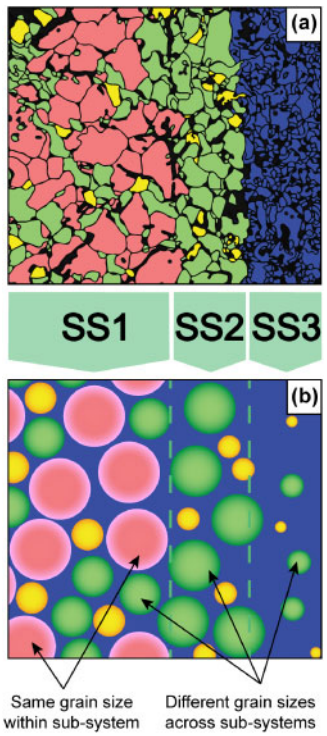

Fig. 3. Schematic illustration of the diffusional re-equilibration model. (a) Mineral grains within a representative volume (spatially rearranged for convenience). (b) Individual grains are approximated as spheres. If there is melt present in the subsystem, the grains are assumed to be fully embedded in melt and keep the spherical shape. Different types of mineral grains will in general have different grain sizes that will evolve according to P–T–c^b conditions (e.g. Ol, Cpx, Opx). Same type of minerals within each subsystem (e.g. every Ol grain within ss1) is modelled with a uniform grain size; however, different grain-size models are allowed across subsystems (e.g. Ol gains in ss1 and ss2 evolve according to different models). (See text for details.)

Diffusion-controlled trace-element model

In contrast to major elements, trace-elements have no explicit thermodynamic control on the interface migration and volumetric free energy changes during phase transformations. Therefore, at least in theory, trace-elements and major-elements can maintain different equilibrium states according to their diffusion kinetics. Here we exploit this property and propose a model for disequilibrium partitioning of trace-elements for reactive transport systems undergoing phase change.

Based on previous studies (Qin, 1992; Iwamori, 1993; Van Orman *et al.*, 2002*a*), we model the disequilibrium partitioning of trace-elements between solid and liquid phases as the combination of two processes: (1) a diffusion-controlled mass flux across mineral grain interfaces and (2) a bulk (volumetric) mass-transfer process resulting from phase changes (e.g. melting or solidification). The former depends on the ability of any given trace-element to diffuse within mineral grains, whereas the later obeys phase transformations as obtained from the DDM model. The trace-element mass exchange occurs within a given representative volume (Fig. 3a). This volume is composed of mineral grains (or thermodynamic phases) formed within the three thermodynamic subsystems (e.g. olivine grains coming from ss1, ss2 and ss3; clinopyroxene grains from ss1, ss2 and ss3, and so on), and an accumulated melt surrounding the mineral grains.

Diffusion within mineral grains is accounted for by introducing a compositional variation in the radial direction of every grain, $c^e_{tp}(r,t)$, which we approximate as spheres (Fig. 3b). Thus, in contrast to the DDM model, the trace-element model explicitly assumes an approximate topology at the micro-scale (Fig. 3b). The concentration of trace element e within a spherical grain of thermodynamic phase tp is given by Fick's second law

$$\frac{\mathrm{D}_s c^e_{tp}}{\mathrm{D}t} = \mathrm{D}^e_{tp}\left(\frac{\partial^2}{\partial r^2} + \frac{2}{r}\frac{\partial c^e_{tp}}{\partial r}\right) \tag{20}$$

where D^e_{tp} is the diffusion coefficient of trace element e within a given mineral grain of thermodynamic phase tp (generally P–T–c^b dependent). The chemical compositions of the solid aggregate can be retrieved by adding individual core-to-rim compositional profiles of every mineral grain.

Regarding the boundary conditions for equation (20), we assume that chemical equilibrium is achieved only at the interface between mineral grains and melt. In other words, the trace-element concentrations in minerals and surrounding melt are linked by the partition coefficient K^e_{tp} only along wet grain boundaries. In addition, because of radial symmetry, the compositional flux across the mineral core should be equal to zero. These conditions read

$$c^e_{tp}|_{r=R_{tp}} = K^e_{tp} c^e_l \tag{21}$$

$$\frac{\partial c^e_{tp}}{\partial r}|_{r=0} = 0 \tag{22}$$

where c^e_l is the liquid's trace-element composition, which is assumed to be locally homogeneous. This assumption is justified as chemical diffusion rates in liquids are much faster than in solid and because the length scale of diffusion for melts is relatively small in comparison with the grain size (e.g. melt at triple junctions).

To be solvable, equation (20) requires additional models for mineral grain size. As local P–T–c^b conditions evolve, mineral abundances and grain-size distributions vary as a consequence of phase trans formations. Mineral phases of the same type but from different sources (i.e. thermodynamic subsystems) are considered to be independent thermodynamic phases with different grain-size evolution models (e.g. olivine grains from subsystems 1, 2 and 3 have different grain sizes; Fig. 3b). On the contrary, mineral grains of the same phase within a given subsystem are assumed to evolve uniformly (e.g. all olivine grains in subsystem 1 have the same grain size, Fig. 3b). Furthermore, we assume that solid grains melt from their outer rims, preserving their spherical symmetry as they dissolve.

A simple model for grain-size evolution of different thermodynamic phases *tp* can be represented by the following equations:

$$\frac{\mathrm{D}_s n_{tp}}{\mathrm{D}t} = n_{tp}\nabla\cdot v_s \tag{23}$$

$$n_{tp} = \frac{\phi_{tp}}{4/3\pi R_{tp}^3} \tag{24}$$

where n_{tp} refers to the number of grains of a given mineral phase per unit of volume (Iwamori, 1993) and ϕ_{tp} is the volume fraction of each of the thermodynamic phase per unit of total volume, which we retrieve from the DDM model. According to equation (23), n_{tp} is advected with the solid velocity and varies exclusively as a consequence of solid-phase compaction or expansion. The number of grains remains constant throughout the simulation (i.e. coalescence and grain division are currently not considered), but the grain size varies according to equation (24). For systems under high shear stresses, this assumption may not be realistic as ductile deformation and associated recrystallization occur during mantle flow (Austin & Evans, 2007). Whereas nucleation of new grains and grain-size reduction enhances chemical equilibrium by increasing the equilibration surface per volume ratio of a given thermodynamic phase, grain growth hampers diffusional re-equilibration. To account for these processes, a 'paleowattmeter' model (Austin & Evans, 2007; Turner *et al.*, 2015), a damage model (Ricard & Bercovici, 2009), or a microscale-model based on Monte-Carlo Potts simulations (e.g. Grose & Afonso, 2019) could be considered. Although such extensions seem possible, they remain challenging from a computational point of view; their implementation and assessment are left for future studies.

From mass-conservation constraints, the mass lost or gained by the mineral grains has to be locally balanced by a corresponding increase or decrease of mass of in the liquid. The conservation of mass of trace element *e* in the liquid phase, c_l^e, is given by an equation similar to equation (7), which in Lagrangian form reads

$$\phi_l\rho_l\frac{\mathrm{D}_l c_l^e}{\mathrm{D}t} = -c_l^e\Gamma + \Gamma^e \tag{25}$$

where

$$\Gamma^e = -\sum\nolimits_{tp}\frac{\mathrm{D}_s}{\mathrm{D}t}\left[n_{tp}\int_0^{R_{tp}}\rho_{tp}4\pi r^2 c_{tp}^e(r)\mathrm{d}r\right] \tag{26}$$

represents the trace-element mass exchange rate. The integral in equation (26) refers to the averaged composition (in volume percent) of trace element *e* within a single mineral grain (e.g. individual olivine grain), which when multiplied by n_{tp}, gives the average composition of trace element *e* of all grains of a given mineral phase (i.e. all the olivine grains within subsystem 1). Equation (26) computes the net rate of trace-element mass loss in the solid by adding the contribution of every thermodynamic phase.

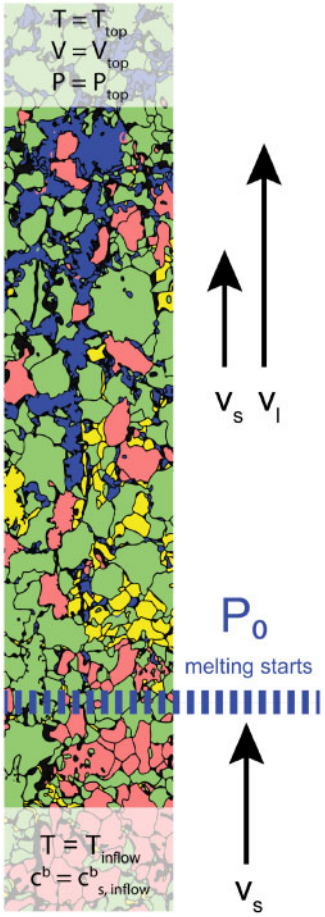

Fig. 4. Conceptual diagram of the one-dimensional mantle column undergoing decompression melting. Boundary conditions on top (e.g. fixed temperature, velocity and pressure) and bottom (e.g. fixed chemical composition and temperature of the inflow material) of the model are indicated. Above the solidus, P_0, solid and liquid (blue) phases move upwards at different velocities v_s and v_l, respectively, according to the TPMCRT model.

In summary, the diffusion-controlled trace element model presented here accounts for the loss or gain of mass of trace element *e* within the solid mineral assemblage as it undergoes both melting or crystallization and diffusional re-equilibration. Conversely, phase-change processes (and their effect on the mineral assemblage, i.e. R_{tp}) are retrieved in an internally consistent manner from the coupling between our thermodynamic model and the grain-size evolution model [equations (23) and (24)]. Also, the extent of disequilibrium between each mineral and melt within each reservoir depends on the efficiency of the diffusional re-equilibration (i.e. initial degree of disequilibrium, equilibration time, grain size and diffusivity), which we estimate via equation (20) and boundary conditions given in equations (21) and (22). Finally, the mineral's gain or loss of trace elements is used to balance the corresponding loss or gain of trace elements in the liquid phase via equation (25). We refer the reader to Appendix A for details on the numerical treatment of the trace element transport modelling.

Table 2: Starting DMM and SD compositions

	c_*^b (wt%)	$c_\dagger^b$ (wt%)		c_*^e (ppb)
SiO_2	44.71	45.94	La	134
Al_2O_3	3.98	5.50	Ce	421
FeO	8.18	7.24	Nd	483
MgO	38.73	28.53	Sm	210
CaO	3.17	10.91	Eu	86
Na_2O	0.13	1.11	Gd	324
Cr_2O_3	0.57	0.04	Dy	471
			Er	329
			Yb	348

*Workman & Hart (2005) .
†Lambart *et al.* (2016).

NUMERICAL EXAMPLES

In this section we explore the basic features of two-phase reactive transport systems by means of one-dimensional numerical simulations of decompression melting (Fig. 4). The modelled mantle column can be thought of as a simplified representation of the rising mantle beneath a mid-ocean-ridge (MOR) axis or beneath a rifting lithosphere. First, the transient behaviour of melt generation and migration is described for a reference case. We then investigate the effects of mantle potential temperature, upwelling rate, chemical disequilibrium and source composition on the modal compositions, melt distribution, energetics and transport in the mantle column. Consequences for the compositional evolution of major and trace elements are discussed in a separate section.

Model setup

The mantle column is modelled as an aggregate of the following.

- Two dynamic phases, namely, liquid (*l*), in this case a melt, and solid (*s*).
- Six thermodynamic phases (*tp*) or minerals, olivine (Ol), clinopyroxene (Cpx), orthopyroxene (Opx), garnet (Grt), spinel (Spl) and plagioclase (Pl). It should be noted that although the liquid is both a thermodynamic and a dynamic phase, here we restrict the use of 'thermodynamic phase' to solid phases only.
- Seven basic components (*b*), SiO_2, Al_2O_3, Cr_2O_3, FeO, MgO, CaO and Na_2O.
- A set of trace elements (*e*) from the rare earth elements (REE) group: La, Ce, Nd, Sm, Eu, Gd, Dy, Er, Yb and Lu.

Table 1 summarizes all the variables used in this study.

Initial and boundary conditions

The 1D numerical domain is 100 km thick. Its initial composition is that of a depleted MORB mantle (DMM; after Workman & Hart, 2005) for both major and trace elements (Table 2). Simulations are initialized with a given adiabatic thermal profile and a 80 km thick thermal boundary layer (TBL) in the upper part of the domain, such that the model is initially melt-free (Fig. 5b and c). The TBL has a linear temperature gradient defined by the surface temperature and the temperature at its base, $T_s = 25\,^\circ$C and T^*, respectively. We test three different values for $T^* = \{1250; 1350; 1450\,^\circ\text{C}\}$, which correspond roughly to mantle potential temperatures of $T_p = \{1224; 1320; 1417\,^\circ\text{C}\}$. Below the TBL, the temperature follows the adiabatic gradient. Temperatures at the upper ($z = 0$ km) and lower ($z = 100$ km) boundaries are held fixed during the simulations (Fig. 4).

We approximate the behaviour of a passive flow (i.e. a regime in which pulling forces at the surface control mantle upwelling) by imposing a constant solid velocity on top of the domain, v_s^{top}, and allowing for passive inflow of mantle through the lower boundary (zero normal gradient). Three different values for $v_s^{\text{top}} = \{1; 5; 10\,\text{cm a}^{-1}\}$ are tested. The incoming mantle at the bottom of the model has a predefined composition $c^b_{s,\text{inflow}}$, and zero melt fraction. For the case of a homogeneous mantle column, $c^b_{s,\text{inflow}}$ is kept constant and equal to the starting DMM composition. For the heterogeneous mantle case, $c^b_{s,\text{inflow}}$ changes to a silica-deficient pyroxenitic composition (SD, after Lambart *et al.*, 2016) 800 kyr after the beginning of the simulation to mimic the arrival of a different mantle lithology.

Numerical simulations are run with a finite-element grid resolution of 300 m and a particle resolution (Lagrangian passive tracers) of ~30 m for solid and liquid compositions. The mechanical problem is solved using a mixed finite-element formulation (Oliveira *et al.*, 2018), whereas the energy and major-element reactive transport problems are solved using the advection–diffusion-reaction algorithm described in Oliveira *et al.* (2016).

Three melting models

Three melting models will be considered here. The first one is the Dynamic Equilibrium Melting (DEM) model, which assumes infinitely fast equilibration rates of major elements within both solid and liquid phases (i.e. $\psi_s = \psi_l = 1$). This effectively means that there is only one subsystem (i.e. ss2) per representative volume (see section 'Extent of equilibration of solid and liquid phases, crystallization and other melting models'). The second model is that of Dynamic Fractional Melting (DFM), where solid and melt evolve in complete chemical isolation (i.e. $\psi_s = 0$ and $\psi_l = 1$) within their corresponding subsystems (i.e. ss1 and ss2, respectively). Lastly, the third and most general model is that of Dynamic Disequilibrium Melting (DDM), which allows for a finite equilibration rate within the solid [i.e. $\psi_s = L_D^s/L_s$ and $\psi_l = 1$, equation (2)]. We remind the reader that by assuming $\psi_l = 1$ in the three melting scenarios, we imply that the diffusion in the liquid phase is fast enough to fully equilibrate with its surrounding solid (i.e. absence of ss3 in any of the explored equilibrium

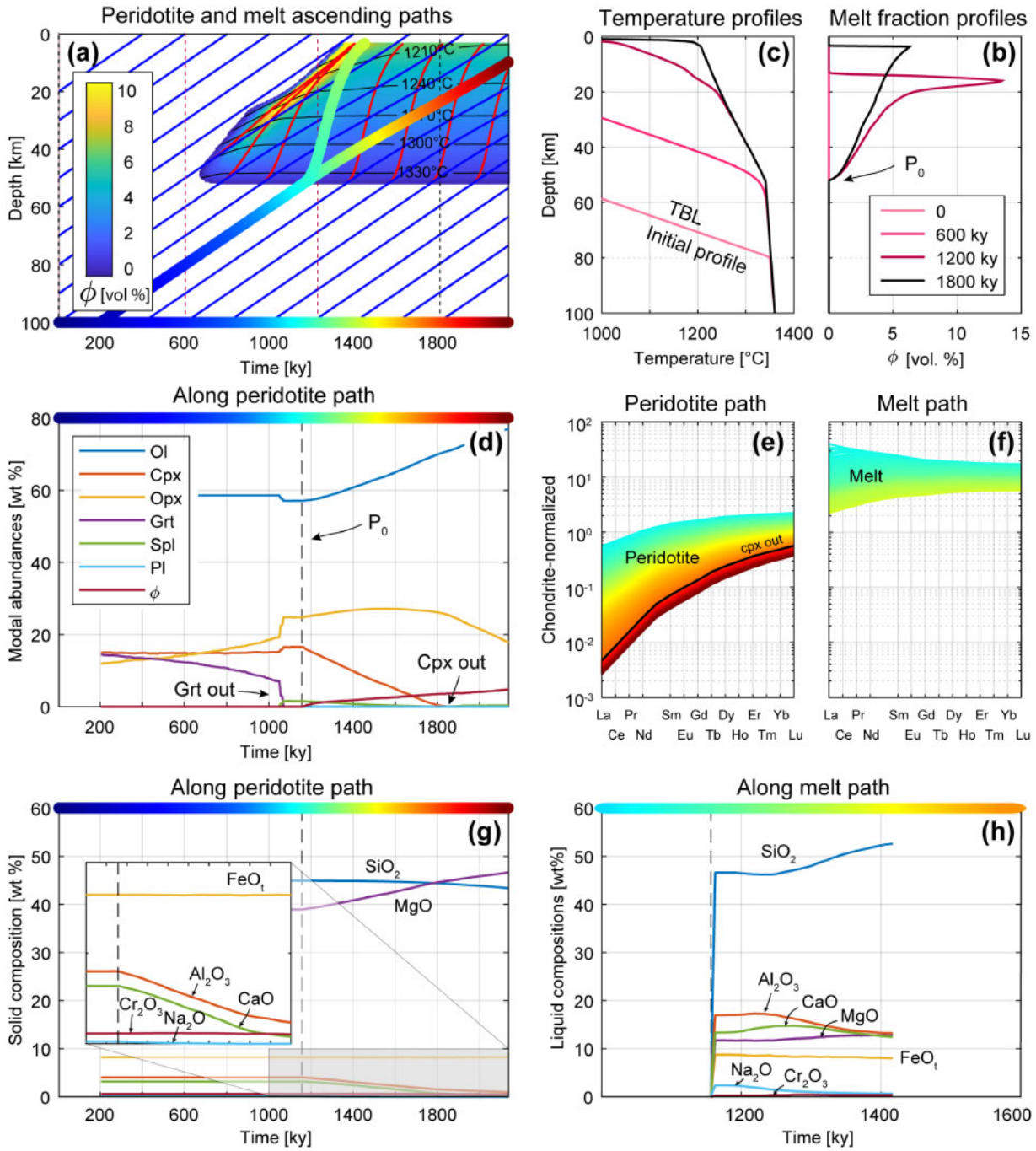

Fig. 5. Evolution of the reference model with $T^* = 1350\,^{\circ}\mathrm{C}$, $v_s^{top} = 5\,\mathrm{cm\,a^{-1}}$ and $\psi_s = \psi_l = 1$. (a) Time evolution of the melt fraction (background color) and temperature (isotherms are indicated by thin black lines) with depth. Ascending *P–T–t* paths of reference peridotites and melts are represented by blue and red lines, respectively. (b) and (c) correspond to melt fraction and temperature profiles for times 0, 600, 1200 and 1800 kyr. (d), (e) and (g) correspond to the evolution of the mineralogical assemblage, trace- and major-element composition along the peridotite *P–T–t* path highlighted in (a). (f) and (h) correspond to the melt's trace- and major-element composition along the liquid *P–T–t* path highlighted in (a). The time dependence of trace-element compositions (e, f) is illustrated with colors according to the scale in (a).

models). Therefore, only two subsystems, ss1 and ss2, need to be tracked in this DDM. However, in contrast to DFM, subsystem ss2 in DDM receives contributions from that fraction of the isolated solid that is allowed to equilibrate with the liquid (as $\psi_s \neq 0$ in DDM). In particular, we assume a very slow equilibration ($D^* = 10^{-20}\,\mathrm{cm^2\,s^{-1}}$) to study scenarios close to complete disequilibrium.

The activity/solution models used in the thermodynamic computations have been given by Jennings & Holland (2015) and/or are available at http://www.perplex.ethz.ch/perplex/datafiles. We refer the reader to Appendix B for additional information on the validation of our thermodynamic implementation, and the underlying Gibbs free-energy minimization procedure.

Reactive transport and trace-element modelling

Model parameters are chosen to represent typical asthenospheric conditions and are generally the same for all the simulations presented here. Heat capacities, densities and closure terms are retrieved from the thermodynamic model via free-energy minimization; other parameter choices are discussed below.

The viscosity of the solid matrix is assumed to follow a diffusion-creep law, $\mu_s = A\exp(E + PV/RT)$ [modified from Hirth & Kohlstedt (2003), where $A = 1{\cdot}8e7$ Pa s, $E = 3{\cdot}75e5$ J mol^{-1}, and $V = 4e-6$ m^3 mol^{-1})], whereas melt viscosity is held constant at $\mu_l = 10$ Pa s. For numerical reasons, and to avoid unrealistically high stresses in cold domains, we use a modified version of the viscosity law, $\mu_s(T) = (1/\mu_s^{diff} + 1/\mu_{max})^{-1}$ where $\mu_{max} = 10^{24}$ Pa s is the maximum allowed viscosity. As given by Bercovici *et al.* (2001), the viscous mechanical interaction coefficient d (c of Bercovici *et al.*, 2001) is modelled as $d = \mu_s\mu_l\phi^2(1-\phi)^2/[\mu_l k(1-\phi)\phi^2 + \mu_s k(\phi)(1-\phi)]$. As $\mu_s \gg \mu_l$, we further simplify d as $\mu_l\phi^2/k(\phi)$. The melt dependence of permeability is given by the low-porosity Kozeny–Carman relationship, $k(\phi) = k_0\phi^n$, where k_0 is the reference permeability set to 10^{-6} m^2 and the permeability exponent to $n = 2$. Therefore, the reference permeability is set to 10^{-10} m^2 at 1 % of melt by volume. The temperature dependence of the thermal conductivity is modelled after Clauser & Huenges (1995), $k_T(T) = A + B/(T + 350)$, where $A = 0{\cdot}73$ W m^{-1} K^{-1} and B = 1293 W m^{-1}.

Partition coefficients are taken from m variables used in this study, Sun & Liang (2014), for Ol, Opx and Cpx, from Johnson *et al.* (1990) for Grt, from Laubier *et al.* (2014) for Plg and from Kelemen *et al.* (2014) for Spl (Table 3). We assume a reference radius for each type of mineral, $R_{tp} = \{3; 1; 2{\cdot}5; 1; 1; 1\}$ mm, and a reference number of grains per unit of volume $n_{tp} = \{5{\cdot}3; 36; 3{\cdot}8; 23{\cdot}9; 9{\cdot}5; 23{\cdot}9 \times 106\}$ m^{-3} for Ol, Cpx, Opx, Grt, Spl and Plg mineral grains, respectively. Experimentally determined REE diffusivities are found in Table 4. These are temperature- and pressure-dependent (Arrhenius relations) for Grt (Van Orman *et al.*, 2002*b*); temperature, pressure and ionic radii dependent [i.e. increasing from light REE (LREE) to heavy REE (HREE)] for Cpx (Van Orman *et al.*, 2001) and temperature-dependent for all other minerals (Cherniak, 2003, for Opx, Plg and Spl; Cherniak, 2010, for Ol). When specified, infinitely fast diffusivities have also been used to test the effect of diffusion on trace-element fractionation.

Table 3: Mineral/melt partition coefficients

	K_{Ol}*	K_{Cpx}*	K_{Opx}*	K_{Grt}†	K_{Plg}‡	K_{Spl}§
La	0·00000092	0·0408	0·00043	0·0016	0·038	0·0006
Ce	0·0000073	0·0876	0·0016	0·005	0·034	0·0006
Nd	0·000058	0·1878	0·006	0·052	0·0302	0·0006
Sm	0·00029	0·3083	0·0158	0·25	0·0214	0·0006
Eu	0·00055	0·3638	0·0227	0·4	0·378	0·0006
Gd	0·0010	0·4169	0·0315	0·85	0·0126	0·000825
Dy	0·0029	0·5034	0·0549	2·2	0·012	0·0015
Er	0·0066	0·5437	0·0808	3·6	0·0073	0·003
Yb	0·0121	0·5453	0·1036	6·6	0·0026	0·0045

*Sun & Liang (2014).
†Johnson (1998).
‡Laubier *et al.* (2014).
§Kelemen (2003).

The reference case

This simulation is initialized with $T^* = 1350$ °C, $v_s^{top} = 5$ cm a^{-1} and $\psi_s = \psi_l = 1$ (i.e. DEM model). Figure 5 summarizes the general evolution of the system, from early melt generation and migration (i.e. roughly approximating rifting stages) to a steady-state situation (i.e. comparable with a mature ridge).

The ascending solid mantle (blue continuous-line P–T paths in Fig. 5a) first intersects the solidus, P_0, at a depth of ∼49 km and a temperature of ∼1320 °C, 679·6 kyr after the beginning of the experiment. As mantle portions from different depths (ascending blue lines with white background color) intersect the solidus, partial melting and melt migration take place. Melt migration or segregation is indicated in Fig. 5a by the different ascending trajectories followed by peridotites (in blue) and melts (in red). Owing to compaction of the solid matrix, the upwelling velocity of the solid decreases (from an initial 5 cm a^{-1} to 1·1–1·7 cm a^{-1} in the shallow part of the melting regime) and that of the fluid increases (up to about 30 cm a^{-1}). The maximum difference in solid and melt velocities increases as the upper part of the melting column reaches shallower depths owing to the upwelling of hot material. Consequently, melts accumulate in the upper part of the melting column (maximum melt fractions of ∼25 % in Fig. 5a, and Supplementary video; supplementary material is available for downloading at http://www.petrology.oxfordjournals.org). Because of the constant temperature boundary condition at the top of the model (thermal lid), these melts slow down and freeze at shallower depths before they reach the upper part of the column.

The evolution of the thermal profile is controlled by the upwelling velocity of mantle material, the depth of the solidus (P_0), the release of latent heat of melting, and the imposed thermal lid (Fig. 5c). Solid mantle first rises along a melt-free adiabat of ∼0·4 °C km^{-1}. When partial melting begins, this adiabat becomes steeper than the melt-free one owing to the consumption of latent heat.

Figure 5d shows the mineralogical changes in the solid along the P–T–t path highlighted in Fig. 5a. As expected, Cpx is progressively removed from the residue as melting proceeds. On the contrary, Ol and Opx increase at elevated pressures, whereas the melting reaction consumes Opx at shallower depths (i.e. lherzolitic to harzburgitic compositions). Accordingly, the major-element composition of this upwelling peridotite becomes increasingly more refractory, with SiO_2 content decreasing at increasing MgO (Fig. 5g). In addition, modelled REE concentrations (Fig. 5e) become

Table 4: Diffusion parameters

	D_{Ol}[1]		D_{Opx}[2]		D_{Plg}[3]		D_{Spl}[1]	
	D_0 ($m^2 s^{-1}$)	ε (kJ mol^{-1})	D_0 ($m^2 s^{-1}$)	ε (kJ mol^{-1})	D_0 ($m^2 s^{-1}$)	ε (kJ mol^{-1})	D_0 ($m^2 s^{-1}$)	ε (kJ mol^{-1})
La	8·0e–10	289	1·2e–7	369	1·1e–2[4]	464[4]	8·0e–10	289
Ce	8·0e–10	289	1·2e–7	369			8·0e–10	289
Nd	8·0e–10	289	1·2e–7	369	2·4e–2[4]	477[4]	8·0e–10	289
Sm	8·0e–10	289	1·2e–7	369			8·0e–10	289
Eu	8·0e–10	289	1·2e–7	369	1e–7[5]	268[5]	8·0e–10	289
Gd	8·0e–10	289	1·2e–7	369	[4]	[4]	8·0e–10	289
Dy	8·0e–10	289	1·2e–7	369	7·1e–3[4]	461[4]	8·0e–10	289
Er	8·0e–10	289	1·2e–7	369			8·0e–10	289
Yb	8·0e–10	289	1·2e–7	369	3·2e–1	502	8·0e–10	289

	D_{Cpx}[6]			D_{Grt}[6]	
	D_0 ($m^2 s^{-1}$)	ε (kJ mol^{-1})	V ($m^3 mol^{-1}$)	D_0 ($m^2 s^{-1}$)	ε (kJ mol^{-1})	V ($m^3 mol^{-1}$)
La	4·20e–3	519·3	1e–5	2·34e–9	287·7	1e–5
Ce	2·20e–3	508·2	1e–5	2·34e–9	287·7	1e–5
Nd	5·54e–4	483·9	1e–5	2·34e–9	287·7	1e–5
Sm	1·42e–4	460·1	1e–5	2·34e–9	287·7	1e–5
Eu	[7]	[7]	[7]	2·34e–9	287·7	1e–5
Gd	[7]	[7]	[7]	2·34e–9	287·7	1e–5
Dy	9·97e–6	413·6	1e–5	2·34e–9	287·7	1e–5
Er	2·73e–6	390·9	1e–5	2·34e–9	287·7	1e–5
Yb	8·83e–7	371·2	1e–5	2·34e–9	287·7	1e–5

[1]Cherniak (2010).
[2]Cherniak and Liang (2007).
[3]Cherniak (2003).
[4]Interpolated from Cherniak (2003).
[5]Assuming diffusion parameters of Sr in labradorite from Cherniak & Watson (1994).
[6]Van Orman *et al.* (2002b).
[7]Interpolated values.

increasingly more depleted along the path; this depletion is very sensitive to the exhaustion of Cpx, which is the main host of LREE in the solid residue (note the change in the rate of depletion, as indicated by the line spacing in Fig. 5e, when Cpx is exhausted).

Melt composition along the liquid *P–T–t* path highlighted in Fig. 5a evolves towards increasingly MgO- and SiO_2-rich compositions (Fig. 5h). Additional details on the evolution of both major and trace elements are discussed in the Discussion.

After ~2000 kyr, the system reaches steady state, where melting rates and transport rates locally balance each other out. During this stage, compositions remain constant at any given depth.

Model response to changes in potential temperature

Figure 6a.1–5 compares results for different melting columns obtained with $T^* = \{1250; 1350; 1450\,^\circ C\}$ at steady state.

As expected, the initial depth of melting P_0 increases with potential temperature (Fig. 6a.1). There is a slightly positive correlation between the adiabatic gradient and T_p in the melt-free region (~0·36; 0·4; 0·42 °C km^{-1}, for $T^* = \{1250; 1350; 1450\,^\circ C\}$, respectively). Above P_0, different behaviours of the adiabats are observed depending on the melting rate and the latent heat of melting released or absorbed by the different mineral phases present in the assemblages (Fig. 6a.2–4). For $T^* = 1450\,^\circ C$, the exhaustion of Cpx at ~56 km and of Opx at ~37 km result in three distinct 'melt-present' adiabats: a lherzolite-melting interval with ~3·2 °C km^{-1}, harzburgite-melting interval with ~2·5 °C km^{-1}, and a dunite-melting interval with ~1·2 °C km^{-1}. Although not shown in Fig. 6a, Grt is also exhausted at ~61 km, but its latent heat contribution is negligible (i.e melting begins in the grt stability field in this case). In the reference case, melting only occurs within the lherzolite and harzburgite intervals (out of the grt stability field). Within these intervals, we find adiabats with similar slopes to those in the $T^* = 1450\,^\circ C$ case. For $T^* = 1250\,^\circ C$, most of the melting occurs within the lherzolite melting interval, and no apparent change in the adiabat is observed.

Figure 6a.5 shows the impact of T^* on melt content. Higher mantle potential temperatures produce longer melting columns (i.e. deeper P_0) with smaller melt fractions, whereas lower potential temperatures result in shorter melting columns, but with higher local melt fractions. This observation is a consequence of three main factors. First, longer melting columns result in larger velocity differences between the solid and liquid phases, which in turn enhances chemical depletion [see, for instance, fig. 2 of Katz (2008) to see the effect of liquid upwelling velocity on bulk composition]; conversely, smaller velocity differences are observed in shorter columns. In these circumstances, near-batch

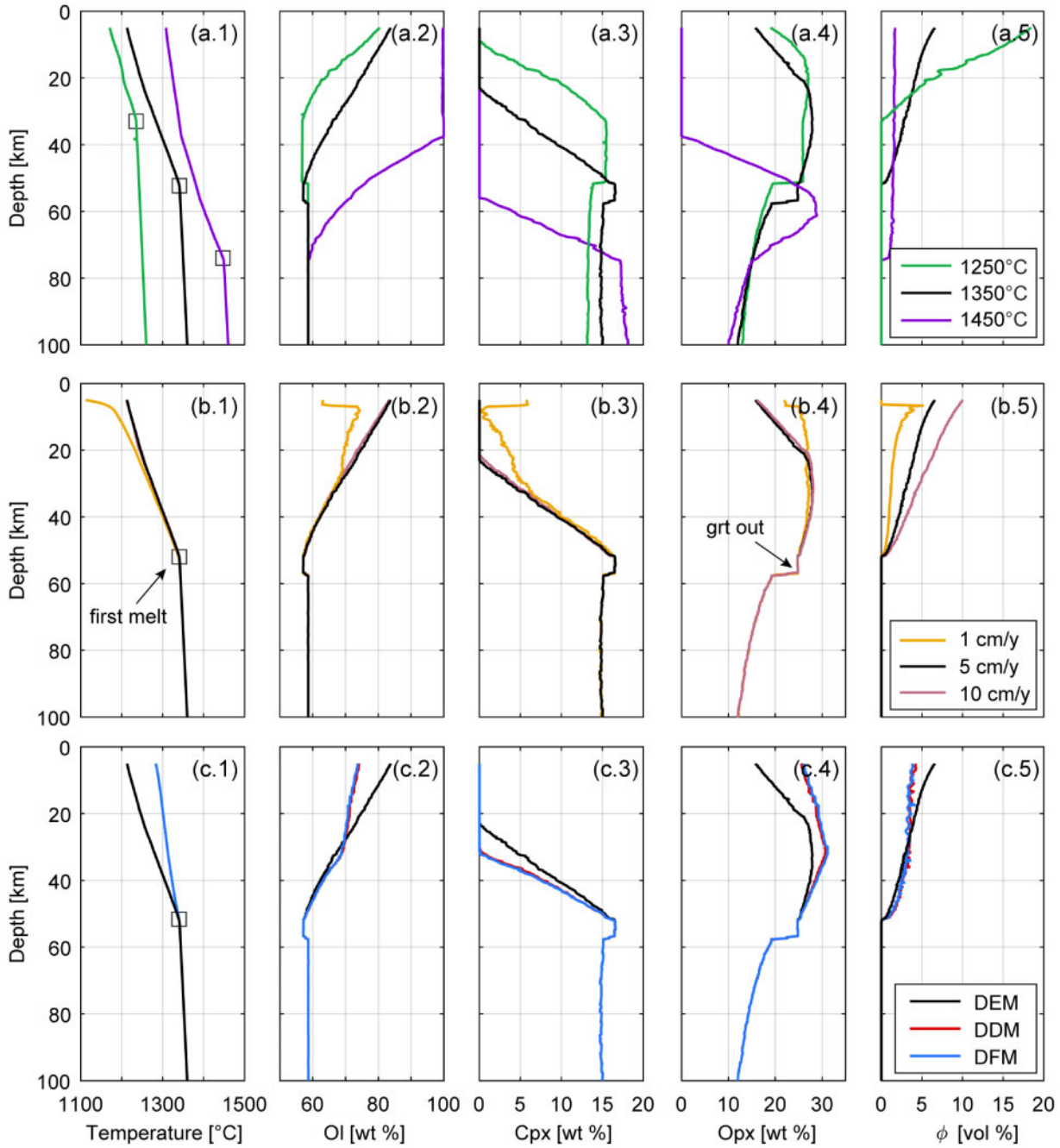

Fig. 6. Predictions from the uniform mantle model for different combinations of parameters. (a.1–a.5) Results for $T^* = 1350 \pm 100\,^{\circ}\mathrm{C}$. (b.1–b.5) Results for $v_s^{top} = \{1; 5; 10\,\mathrm{cm\,a^{-1}}\}$. (c.1–c.5) Results for different ψ_s (i.e. DEM, DDM, DFM). Each column depicts depth profiles of (a.1, b.1, c.1) temperature in °C, (a.2, b.2, c.2) Ol content in wt%, (a.3, b.3, c.3) Cpx content in wt%, (a.4, b.4, c.4) Opx content in wt%, (a.5, b.5, c.5) melt fraction in vol%. (c.2–c.4) refer to bulk solid modal abundances (adding the solid phases in both equilibrated and isolated domains). Results within the equilibrated domain (i.e. ss2) and isolated solid domain (i.e. ss1) are reported for different disequilibrium scenarios in Fig. 7.

melting conditions are approached (i.e. melt fraction approaching the degree of melting, $\phi \approx F$). Second, deeper melting caused by higher mantle potential temperatures implies 'early' depletion of the solid residue, whereas more fertile mantle material is able to reach shallower depths when lower potential temperatures are used. Lastly, on a cold adiabat, relatively fertile lithologies are able to reach and melt at shallow depths (in the plagioclase lherzolite stability field), which generates a high melt productivity pulse and large melt fractions.

Model response to changes in upwelling velocity

We run two additional simulations where the upwelling rate is set to 1 and 10 cm a^{-1} (compare with the 5 cm a^{-1} rate used in the reference case); all other parameters are the same as in the reference case. This range of

upwelling velocities is well within those observed in medium- to fast-spreading mid-ocean ridges (Niu & Hekinian, 1997).

Temperature, mineral modes and degree of melting are insensitive to variations in the flow field when a 1D steady-state melting column in equilibrium (and in absence of diffusion in the energy equation) is considered (Ribe, 1985; Katz, 2008; and discussion below). This is evident in Fig. 6b.1–4, where fast mantle upwelling columns exhibit very similar temperature and mineral mode profiles. In these cases, the effect of heat conduction is negligible in comparison with heat advection (i.e. the length of the thermal boundary layer becomes negligible), and the model effectively recovers the assumptions stated above. On the contrary, heat conduction within the thermal boundary layer becomes prevalent in slower systems, as reflected in the different temperature and mode profiles compared with the reference solution (Fig. 6b.1–4).

Despite having similar temperature and mineral mode profiles, the local melt fraction along the melting column increases with upwelling rate (Fig. 6b.5). This is due to the well-known relationship between upwelling and melting rate (i.e. $\Gamma \approx -\rho v \partial F/\partial z$, Asimow & Stolper, 1999), which, as mentioned above, also affects the bulk composition of the system with depth without affecting individual compositions of melt and solid residues at a given depth.

Model response to disequilibrium

Figure 6c.1 shows that disequilibrium cases (DDM and DFM) reach hotter steady-state solutions than the equilibrium case (DEM). In addition, and despite being hotter, melt fraction along the melting column decreases for increasing extents of disequilibrium (Fig. 6c.5). Both observations are explained by the lower degree of melting of chemically isolated solids (i.e. ss1 subsystem; see discussion below): on the one hand, it results in lower melt fluxes (i.e. lower melt fractions); on the other, in less consumption of latent heat of melting (i.e. higher temperatures).

Although DDM and DFM show similar temperature profiles, the mineralogical evolution differs between disequilibrium models (Figs 6c.2–4 and 7); it should be noted that Fig. 6c.2–4 refers to the bulk mineralogy (i.e. taking into account the solid phases within ss1 and ss2), whereas Fig. 7 illustrates the mineral phase distribution within each of the equilibrated (top panels) and isolated (bottom panels) domains. In the case of complete disequilibrium (DFM), ss2 is mostly above the liquidus (i.e. $\phi_{ss2,s} = 0$ in Fig. 7a), whereas with a finite equilibration rate, DDM results in the formation of mostly Ol in equilibrium with the melt (Fig. 7a). The amount of solid in equilibrium with the melt linearly increases with depth (Fig. 7a), making up to 35% of the total ss2 domain at shallow depths (computed as $\phi_{ss2,s}/(\phi_{ss2,s} + \phi_l)$, not shown). Because in the DDM scenario portions of the isolated solid equilibrate within ss2 at every time step, the ss1 domain becomes significantly smaller at decreasing depths (Fig. 7b). Both disequilibrium cases show almost identical mineral assemblages within the isolated solid domain (ss1, Fig. 7b), as it is the same initial solid source that melts without any further equilibration along similar *P*–*T* paths (Fig. 6c.1).

Model response to a heterogeneous source

Figure 8 summarizes the evolution of a system identical to the reference case, but including the inflow of a silica-deficient pyroxenitic composition (SD pyroxenite) at the base of the column, 800 kyr after the beginning of the simulation (see corresponding video in the supplementary material).

Results in Fig. 8 suggest that the evolution of the one-dimensional melting column can be divided into three time intervals. The first one corresponds to the time between the formation of the first peridotite melt (677 kyr) and that of the first pyroxenite melt (1473 kyr). Because the upwelling pyroxenite remains below its solidus during this interval, the system behaves as described for the Reference Case.

The second interval corresponds to that when both peridotites and pyroxenites melt simultaneously, but without direct chemical interaction between them. The pyroxenite intersects its solidus at a depth of ~67 km and a temperature of ~1345 °C (P_0, Fig. 8a). Above the solidus, pyroxenitic melts interact with, and percolate through, other pyroxenites, but do not interact with any peridotite residue (the two melting columns are not interconnected yet; Fig. 8a). Unlike what happens in the peridotite melting column, these pyroxenitic melts do not freeze, but encounter an unmolten (impermeable) peridotite solid that impedes any further upward migration. In principle, pyroxenitic melts could percolate through unmolten peridotites along pre-existent porosity pathways. However, our numerical model considers porosity and melt fraction to be equivalent, which means that porosity cannot be created without melting. Consequently, the peridotite acts as a chemical permeability barrier for the pyroxenitic melt, which forces both pyroxenitic melts and solid residues to travel upwards at the same rate. This in turn implies that batch melting is favoured on top of the pyroxenite melting column ($F = \phi$), leading to an accumulation of high volume fractions of pyroxenitic melts in this domain (Fig. 8a–c).

Because the pyroxenitic body begins to melt at deeper levels than the peridotitic mantle, the thermal profile develops two distinct temperature gradients, one for each melting column (Fig. 8b, 1800 kyr). Our results show that the heat diffusion below the peridotite solidus enhances melting on top of the pyroxenite melting column (Fig. 8c). In turn, pyroxenite melting induces undercooling of the peridotitic mantle, owing to consumption of latent heat by melting of the low-*T*-solidus

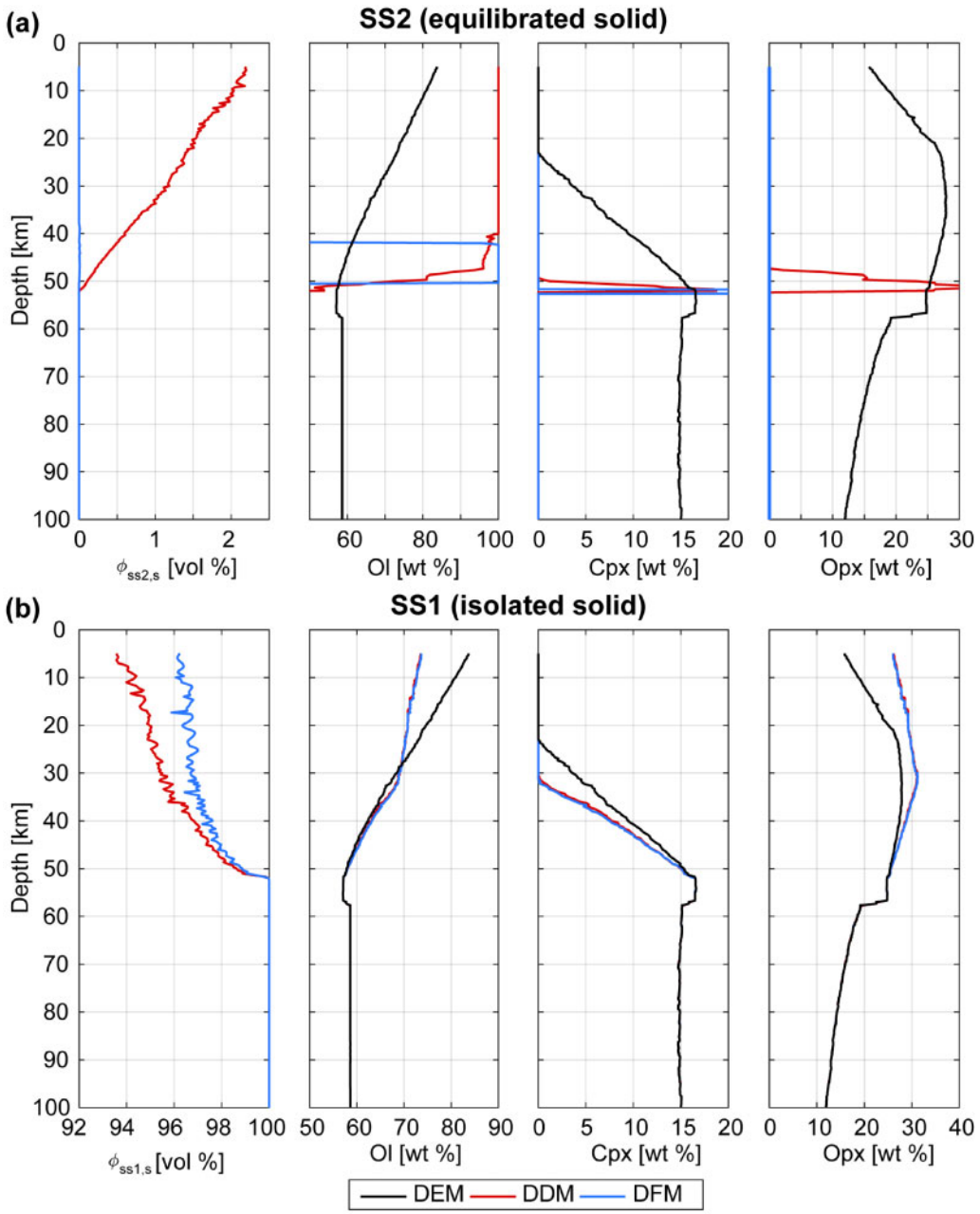

Fig. 7. Predictions from the uniform mantle model for the solid residue within both (a) the equilibrated domain (ss2) and (b) isolated solid domain (ss1) for DEM, DDM and DFM models. From left to right, each column depicts depth profiles of equilibrated and isolated solid volume fraction, Ol content in wt%, Cpx content in wt% and Opx content in wt%. Mineral phase wt% values are computed as weight fractions within each thermodynamic subsystem.

pyroxenites (see 'Model caveats and further developments' for further discussion). Consequently, we observe a delay in the onset of melting of the peridotite with respect to the reference case (i.e. Fig. 8b and c, and Supplementary video).

Lastly, the third time interval begins once the temperature on top of the pyroxenitic melting column reaches the peridotitic mantle solidus (~1815 kyr). At this point, the two melting columns become connected and form a single mantle melting column, where pyroxenitic melts are allowed to mix with peridotitic melts and migrate through the residual peridotites above. As a consequence of a longer melting column, the upwelling velocity of the solid decreases and that of the fluid increases (red and blue lines in Fig. 8a). Also, the low temperature induced from pyroxenite melting migrates upwards at an intermediate rate (i.e. faster than the upwelling peridotites, but slower than the percolating melts), causing an average drop in temperature of 40 °C ahead of the upwelling pryroxenitic mantle (Fig. 8a and b).

Figure 8d illustrates the consequences of thermal and chemical interaction between pyroxenitic melts and

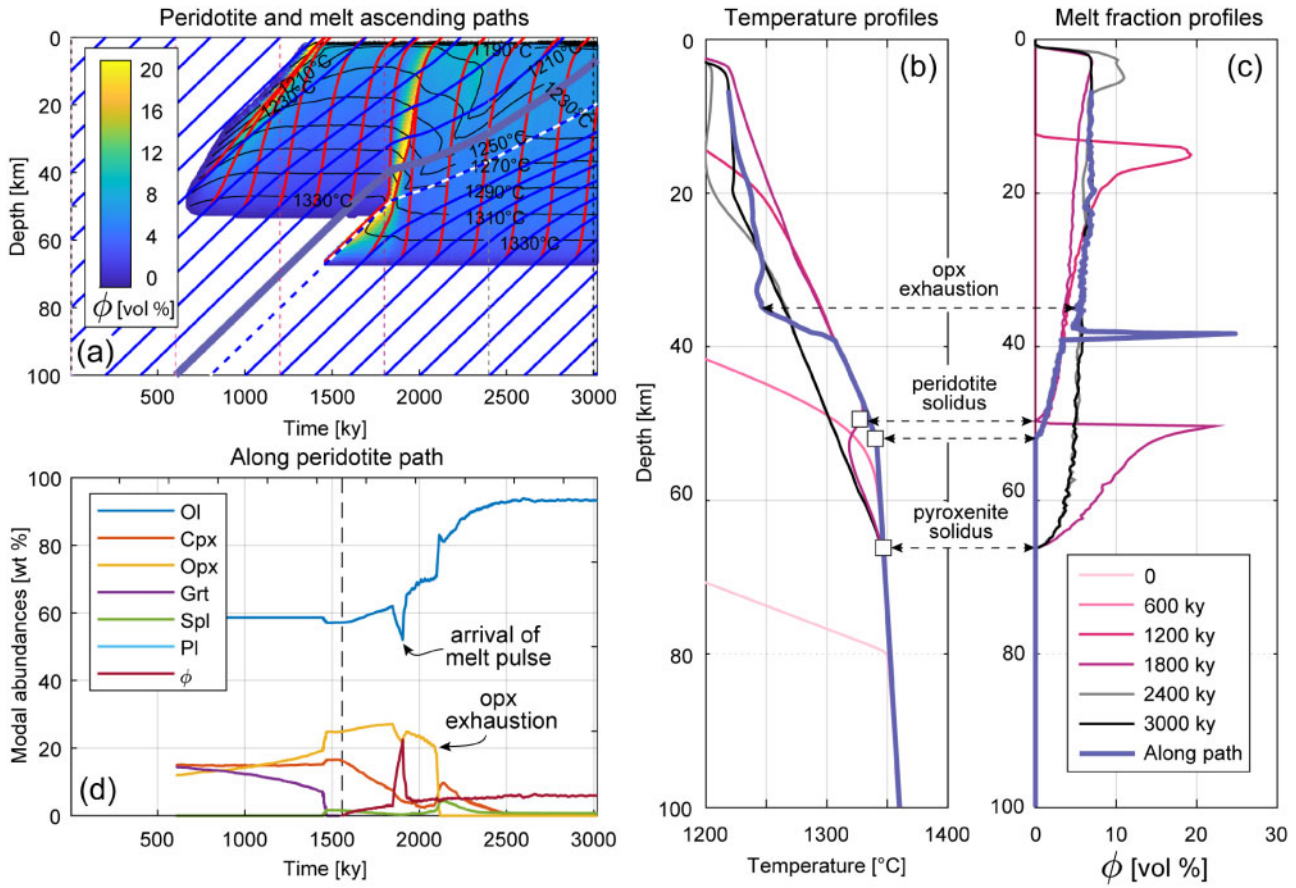

Fig. 8. Evolution of the reference model with a heterogeneous source. SD pyroxenites enter the column from beneath at 600 kyr. (a) Time evolution of the melt fraction (background color) and temperature (isotherms are indicated by thin black lines) with depth. Ascending *P–T–t* paths of reference peridotites and melts are represented by blue and red lines, respectively. (b) and (c) show temperature and melt fraction profiles for times 0, 600, 1200, 1800, 2400 and 3000 kyr. (d) shows the evolution of the mineralogical assemblage along the peridotite *P–T–t* path highlighted in (a).

peridotites on the mineralogy of the peridotitic mantle along the *P–T–t* path highlighted in Fig. 8a. Melting through the first and second interval does not differ much from the reference case. The third interval, however, is characterized by (1) a sudden increase in melt flux, followed by (2) a progressive removal of Opx and (3) a simultaneous increase of Cpx in the solid residue. The high melt flux in the beginning of the third interval corresponds to the release of the accumulated melt in the top of the pyroxenitic melting column. After the passage of this melt pulse, the temperature steadily drops (Fig. 8b) and Opx is progressively removed from the residue, which becomes increasingly Ol-rich. Despite the drop in temperature, melt fractions are 2–3 wt% higher after the arrival of the melt pulse owing to the pyroxenitic melt–peridotitic solid interaction (Fig. 8c). Because of this interaction, a Cpx-rich front (in absence of Opx) develops ahead of the pyroxenitic mantle (Supplementary video), which travels faster than the upwelling solid. The relative upwelling velocities between this Cpx-rich equilibration front (and its associated steeper thermal gradient) and the peridotitic mantle causes the observed increase in local temperature along the peridotite path (see Supplementary video, and Fig. 8b). As the upwelling mantle reaches shallower depths, this newly formed Cpx is progressively removed from the solid residue, temperature decreases (as a consequence of latent heat consumption) and dunitic compositions are obtained (Ol crystallizes as shown in Fig. 8d and Supplementary video). We stop the simulation before the pyroxenitic mantle completely replaces the peridotite and a new effective steady-state solution is reached.

DISCUSSION

Petrological and geochemical implications

Our modelled melts and residual peridotites contain the chemical record of the integrated reaction and transport rates along their respective trajectories through *P–T–c*^{b} space. As such, they are useful to study the generation and evolution of both natural lavas (e.g. MORBs, intraplate lavas) and residual mantle rocks (e.g. abyssal peridotites). In this section we explore the chemical evolution of melts and residual peridotites in response to different model scenarios, such as changes in potential temperature and degree of disequilibrium. Our main goal here is to explore the various causes of

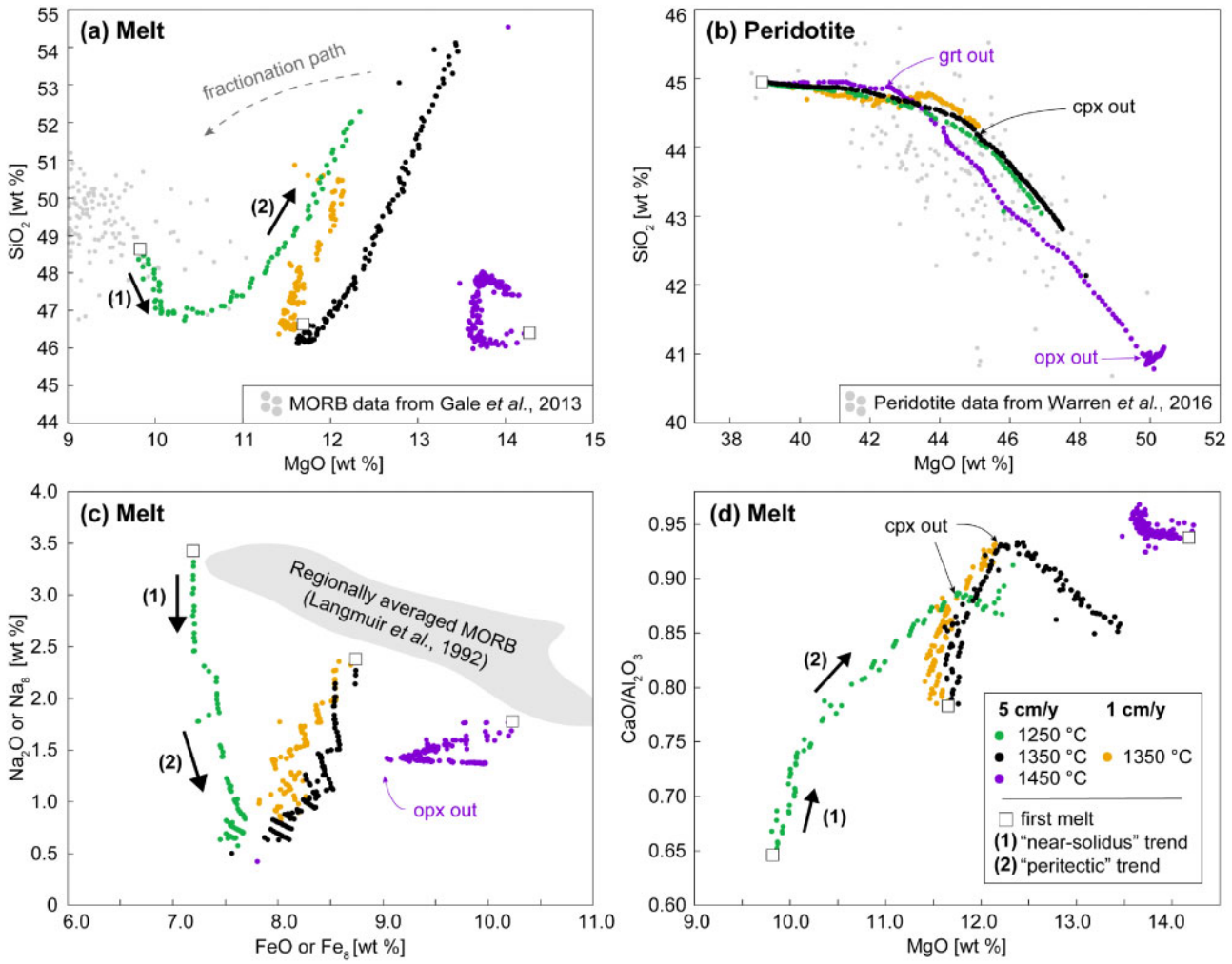

Fig. 9. Compositional evolution of melts (a, c, d) and periodotites (b) along corresponding *P–T* paths in steady state. (a) SiO_2 vs MgO wt% in melts; (b) SiO_2 vs MgO wt% in solids; (c) Na_2O vs FeO wt% in melts; (d) CaO/Al_2O_3 vs MgO wt% in melts. Colored dots refer to model results, whereas grey shading and dots refer to MORB (after Langmuir *et al.*, 1992; Gale *et al.*, 2013) and peridotite data (after Warren, 2016). The discrepancy between MgO content in modelled melts and MORBs is ascribed to ol fractionation at shallow depths experienced by MORBs. No fractionation correction has been applied to our primary compositions but the effect of fractionation is illustrated with the dashed arrow in (a). We refer to Asimow (2001) for considerations regarding imposing arbitrary fractionation paths on a range of modelled primary melts that may follow various liquid lines of descent (LLD). The mismatch of Na_2O content between modelled melts and MORB data is due to the low Na_2O content of the source (Workman & Hart, 2005). First melt compositions and the different melting trends discussed in the text are indicated. It should be noted that the effect of thermal boundary layer on the composition of melts for the case of 1 cm a^{-1} upwelling rate (yellow dots) is similar to the combined effect of increasing the upwelling velocity and lowering the mantle potential temperature (green dots).

compositional variability arising from melting processes in a dynamic situation rather than providing direct constraints on petrogenesis. However, comparisons with experimental data and other parameterized polybaric melting models will be discussed wherever relevant. Other model scenarios, including melting of heterogeneous sources, are briefly discussed in 'Model caveats and further developments'.

The role of potential temperature

The role of potential temperature in major-element chemistry has been the focus of many experimental (e.g. Blundy *et al.*, 1995; Klemme *et al.*, 2002; Falloon *et al.*, 2008) and numerical (e.g. Hirschmann *et al.*, 1998; Asimow, 2001) studies. As shown in 'Model response to changes in potential temperature', T_p controls the initial P_0 and thus the length of the melting column (i.e. the extent of polybaric melting), which in turn controls the magnitude of differentiation that occurs by reactive melting. For instance, primary melts generated at higher temperatures are MgO-richer and SiO_2-poorer than their lower temperature counterparts (Fig. 9a), which is due to the increase in the melting modes of Ol with decreasing pressure (O'Hara, 1968; Stolper, 1980).

As melting proceeds, we observe an initial decrease in SiO_2 as MgO increases (Fig. 9a; $T^* = 1450\,^{\circ}C$ is an exception, as melting begins in the garnet stability field). This decrease in SiO_2 is mostly owing to the high SiO_2 content of near-solidus melts. Because subsequent melt increments are further away from the solidus (i.e. less

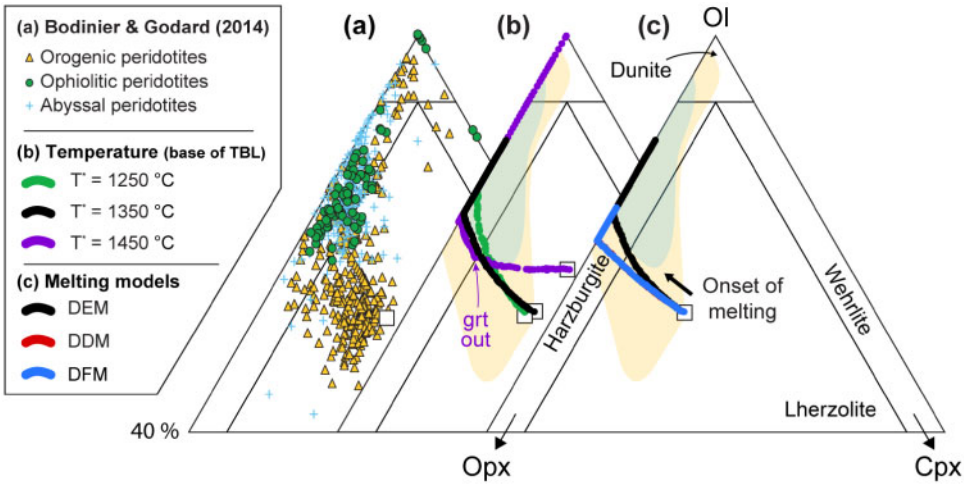

Fig. 10. Modal compositions of (a) abyssal, ophiolitic and orogenic peridotites compiled by Bodinier & Godard (2014), compared with modelled peridotites from (b) $T^* = \{1250; 1350; 1450\,^{\circ}C\}$ and (c) DEM, DDM and DFM models in steady state, plotted into the peridotite field of the Ol–Opx–Cpx diagram (Streckeisen, 1976).

SiO_2 enriched), pooling of these melts along the melting P–T path results in the observed SiO_2 decrease. The enrichment of near-solidus melts is consistent with experiments, and is a consequence of their high alkali contents, Na_2O in this case (Hirschmann *et al.*, 1998; Robinson *et al.*, 1998; Wasylenki *et al.*, 2003). However, Fig. 9a also shows that this initial SiO_2 enrichment varies with T_p. Indeed, high pressures enhance the stabilization of the jadeite component of cpx (Blundy *et al.*, 1995), which leads to larger K_{Cpx}^{Na} values (e.g. Baker *et al.*, 1995; Hirschmann *et al.*, 1998; Falloon *et al.*, 2008). Consequently, the initial Na_2O enrichment (and in turn, the initial SiO_2 enrichment) is less marked in melts obtained at high pressures (i.e. high potential temperatures).

After the initial SiO_2 enrichment of near-solidus melts (hereafter referred to as the 'near-solidus' trend), primary melts evolve towards increasingly MgO- and SiO_2-rich compositions. This positive correlation between MgO and SiO_2 can be better understood in the simplified CaO–MgO–SiO_2 (CMS) system. As the melting mode of Ol increases with decreasing pressure, enstatite (En) melts incongruently (En $\Rightarrow$ Fo + SiO_2) at pressures $<1{\cdot}4$ GPa (Morse, 1980). Low-pressure melting of a lherzolitic composition then occurs at the peritectic temperature and the melt composition remains that of the peritectic point until diopside is removed from the residue. With decreasing pressure, the peritectic composition is progressively shifted towards higher SiO_2 and the peritectic temperature is lowered, as demonstrated by Niu (1997). However, as transport drives the system towards lower pressure, each melt increment is in increasing thermal and chemical disequilibrium with respect to the peritectic point. While the peritectic composition itself evolves towards higher SiO_2 and lower MgO at decreasing pressure, the peritectic reaction in this dynamic situation results in melt compositions driven not only towards higher SiO_2, but also towards higher MgO (Fig. 9a). We refer to this melting interval characterized by the positive correlation between SiO_2 and MgO as the 'peritectic' trend.

In the Na_2O–FeO systematics, primary melts obtained for higher T_p have lower Na_2O and higher FeO contents (Fig. 9c), which coincides with the global trend of regionally average MORB in Na_8 vs Fe_8 space (Klein & Langmuir, 1987). The correlation between Na and Fe varies with T_p (Fig. 9c). High T_p shows a positive correlation, whereas low T_p (e.g. $T^* = 1250\,^{\circ}C$) results in slightly negative correlation. This evolution is a direct consequence of the P–T dependence of the peritectic melting reaction described above. Our observations are consistent with earlier forward thermodynamic models (e.g. Asimow, 2001) and support the interpretation of positive Na_8 and Fe_8 correlations as indicative of local MORB trends occurring at the ridge-segment scale (Klein & Langmuir, 1989). In this regard, individual basalts within a given suite could effectively sample different portions of the melting regime (i.e. melt extraction from different parts of the underlying melting column). Whether this interpretation is reasonable is beyond the scope of this paper, and so is the debate on the origin of the global versus local MORB trends (e.g. Dick & Zhou, 2015). However, this interpretation requires local MORB trends to be associated with a systematic decrease in MgO—a piece of information that is lost when only data normalized to 8% MgO is considered. This topic is further discussed in 'The Consequences of Disequilibrium'.

Regarding the residual peridotite, Fig. 9b shows good agreement between our modelled melting residues and the characteristic negative correlation between SiO_2 and MgO of abyssal peridotites (e.g. Warren, 2016). We note that T_p has little influence on the SiO_2 vs MgO trends in the solid; Si depletion tends to be only slightly stronger for lower T_p. The hottest case ($T^* = 1450\,^{\circ}C$) is an exception because melting is

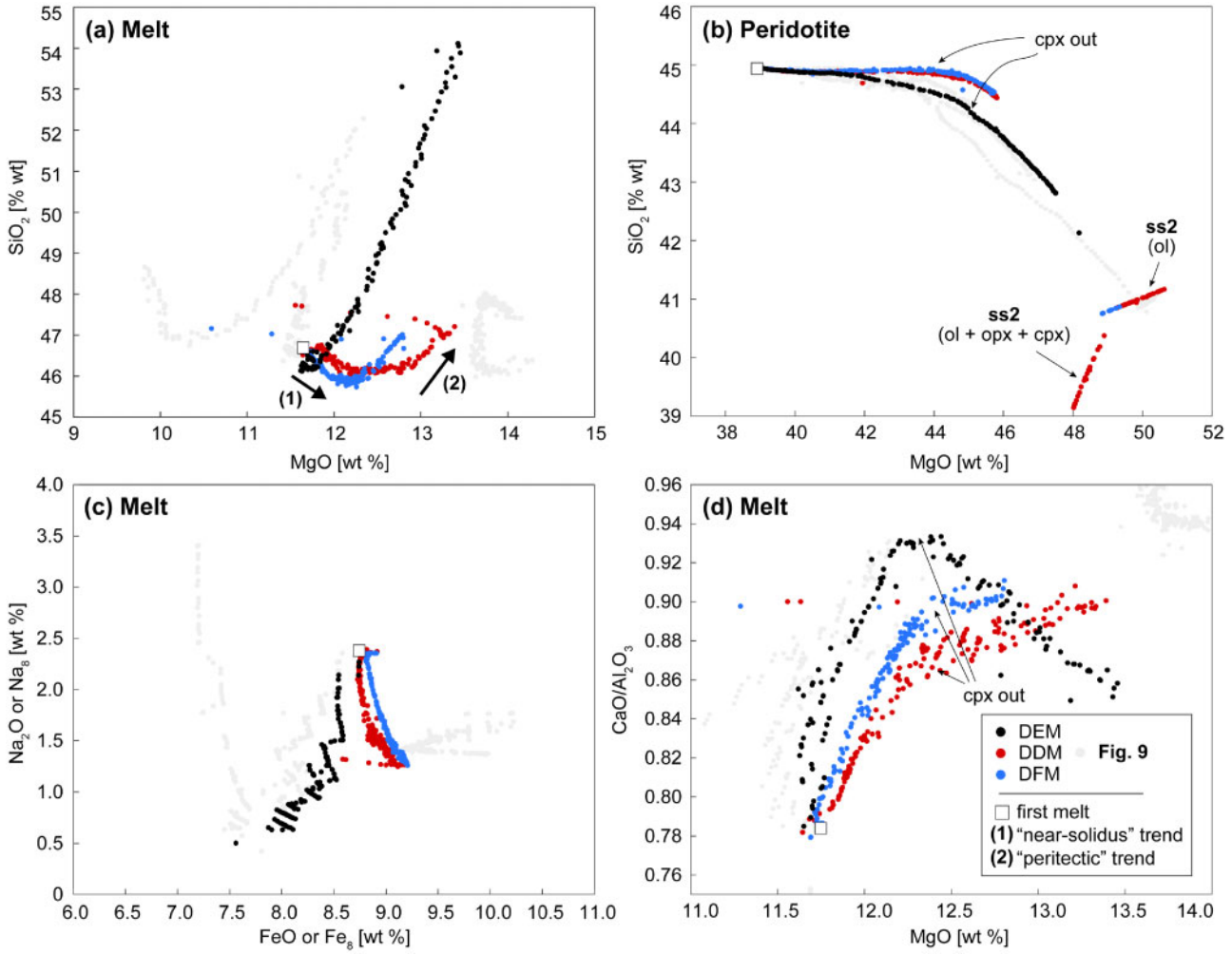

Fig. 11. Compositional evolution of melts (a, c, d) and periodotites (b) along corresponding *P*–*T* paths in steady state and for different degrees of equilibrium. (a) SiO_2 vs MgO wt% in melts; (b) SiO_2 vs MgO wt% in isolated solids (within ss1) and equilibrated solids (within ss2); (c) Na_2O vs FeO wt% in melts; (d) CaO/Al_2O_3 vs MgO wt% in melts. Colored dots refer to DEM, DFM and DDM model results, whereas grey dots in the background refer to model results shown in Fig. 9. The first melts and the different melting trends discussed in the text are indicated.

initiated in the garnet peridotite stability field. In this case, SiO_2 initially remains nearly constant, and then sharply decreases (upon Grt exhaustion) until Opx is completely exhausted. The negative correlation between SiO_2 and MgO (and between FeO and MgO) is sometimes used as evidence for the addition of Ol to fractional-melting residues at shallow depths (Niu, 1997, 2004). However, our results align with other equilibrium transport models (e.g. Asimow, 2001) and suggest that the major-element systematics of abyssal peridotites can be explained exclusively by partial melting. This conclusion is valid to a first order, provided that the process occurs over a sufficiently long melting column and in chemical equilibrium. Furthermore, Fig. 10a and b shows that most of the range of lherzolitic to harzburgitic compositions of abyssal peridotites are satisfactorily reproduced by our model (dunitic residues are only obtained in the hottest scenario). Trace-element compositions of both modelled melts and peridotites in equilibrium are discussed and compared with their disequilibrium counterparts in the next section.

The consequences of disequilibrium

Major-element systematics. Results obtained in disequilibrium cases (i.e. DDM and DFM) show that the degree of chemical disequilibrium significantly modifies the compositional trends of major elements when compared with their equilibrium counterpart (Figs 10 and 11).

Compared with the equilibrium situation described above, near-solidus trends can be observed over longer melting intervals. Because melts are constantly removed from the isolated solid domain (ss1), every new melt increment formed in equilibrium within ss1 is in fact very close to a near-solidus melt. This is especially true as low melt fractions are maintained throughout

the column (Fig. 7). Consequently, the aggregated melt compositions tend to approach those of instantaneous near-solidus melts. This is the reason why the near-solidus trend of SiO_2 in Fig. 11a takes place over a wider range of MgO contents than in the equilibrium scenario . Also, owing the stronger partitioning of Na_2O in near-solidus melts (Hirschmann *et al.*, 1998; Robinson *et al.*, 1998; Wasylenki *et al.*, 2003), Na_2O and FeO become negatively correlated in the disequilibrium cases (Fig. 11c). This observation contrasts with the positive correlation obtained in the reference equilibrium model and suggests that for equal potential temperature, source composition and upwelling rates, the slope of the Na_2O–FeO trend can change from negative (as in the global MORB trend) to positive (as in local MORB trends) solely out of disequilibrium.

Another difference from equilibrium scenarios is that the compositional differentiation that occurs during the peritectic melting interval is less marked. Modelled melt compositions are restricted to ~46–47 wt% SiO_2 in disequilibrium, while they reach 54 wt% in DEM models (Fig. 11a). We also observe that the greater the chemical disequilibrium, the lower the SiO_2 content of primary melts (Fig. 11a). Similarly, complete disequilibrium (i.e. DFM) restricts the range of MgO content of melts (Fig. 11a). However, the sluggish diffusional re-equilibration permitted in the DDM model ($D^* = 10^{-20}\,cm^2\,s^{-1}$) is enough to recover the range of MgO content obtained in DEM.

FeO also becomes positively correlated with MgO in disequilibrium cases (which can be inferred comparing Fig. 11a and c). This observation is counter-intuitive from the point of view of simple batch and fractional melting models, but is nonetheless important, as higher Fe_8 values in the final melts have been associated with deeper melting (Klein & Langmuir, 1987). In this particular case, the positive correlation between FeO and MgO is only a consequence of the restricted melt–peridotite interaction that arises from disequilibrium. In this context, disequilibrium produces a comparable effect with that obtained from the focused-melting model of Dick & Zhou (2015) whereby residues are incrementally removed from the system.

We also note that disequilibrium significantly modifies the modelled CaO/Al_2O_3 ratio in melts (Fig. 11d). For as long as Cpx remains in the residue, equilibrium melting yields partial melts with greater CaO/Al_2O_3 ratios. After Cpx exhaustion, CaO/Al_2O_3 continues to increase (although less steeply) in both DDM and DFM, whereas it sharply decreases in DEM. (Hirschmann *et al.*, 1999) demonstrated that more depleted sources counter-intuitively produce melts with higher CaO and CaO/Al_2O_3 (at a given *P*, and for relatively low *F*). Hirschmann *et al.* argued that this behavior occurs because CaO in melt is dependent upon temperature and the alkali content of the melt, especially near the solidus. Interestingly, disequilibrium affects both temperature (e.g. higher temperatures) and near-solidus melting (e.g. longer near-solidus melting intervals), which results in less CaO entering the melt during the lherzolite melting interval. The observed lower CaO/Al_2O_3 ratios in disequilibrium cases are thus caused by the combined effect of higher temperatures (which narrow the En–Di solvus), and the prevalence of near-solidus melts whose high Na/Al stabilizes Ca-rich silicate phases (George & Stebbins, 1996). For the same reason, by the time Cpx is exhausted in disequilibrium cases, the residues have been less depleted in CaO in DDM and DFM, and further melting results in a continuous increase in CaO/Al_2O_3 (which still remains lower than in DEM at comparable *F*; Fig. 11d). Our results thus align with Hirschmann *et al.* (1999) and Asimow (2001) in ascribing the variability in CaO/Al_2O_3 to changes in source composition and temperature, but also illustrate the important role of disequilibrium in the complex thermo-chemical feedbacks leading to particular CaO/Al_2O_3 ratios. These considerations suggest that some caution is necessary for quantitative interpretation of CaO/Al_2O_3 ratios of basalts, which have been often proposed as a reliable indicator of the extent of melting (Niu & Hekinian, 1997).

Following from the modelled melts, solid compositions arising from disequilibrium scenarios are less melt-depleted in major elements than those obtained in equilibrium (see SiO_2 vs MgO in Fig. 11b). Similarly, a higher Opx/Ol ratio is observed at a given modal abundance of Cpx as a result of the enhanced near-solidus melting trends discussed above (Fig. 10c). These observations are only slightly sensitive to the imposed extent of disequilibrium (i.e. similar trends of major-element and modal compositions are observed in DDM and DFM). However, it is worth noting that the two disequilibrium cases are distinguished by the presence of two distinct mineral assemblages within subsystem 2 (i.e. the subsystem composed of the melt and any solid in equilibrium with it; Fig. 7a). In complete disequilibrium (i.e. DFM), this equilibrated solid is only found within the first ~9 km of the melting column (and in very low volume fraction), whereas it is present across the whole melting column if some extent of equilibration is permitted (Fig. 7a). This equilibrated solid consists essentially of crystallizing Ol in DFM and Ol with pyroxenes ± Spl in DDM, particularly at depths near the solidus (Figs 7a and 11b). This result indicates that, in a situation where melting and melt migration occur at least partly in disequilibrum, Ol-rich lithologies can be expected to crystallize in low-volume in the asthenospheric mantle. On this basis, we suggest that the formation of wehrlite and Ol- gabbro documented in the mantle section of ophiolites (e.g. Python & Ceuleneer, 2003; Herzberg, 2004, and references therein) could be the result of this process occurring during melt extraction below mid-ocean ridges. This interpretation is consistent with the spatial relationships observed in some occurrences between such lithologies and dunite channels (e.g. Piccardo & Guarnieri, 2010), where it is assumed that dunite channels had favoured the development of focused melt flow (and thus partly in disequilibrium).

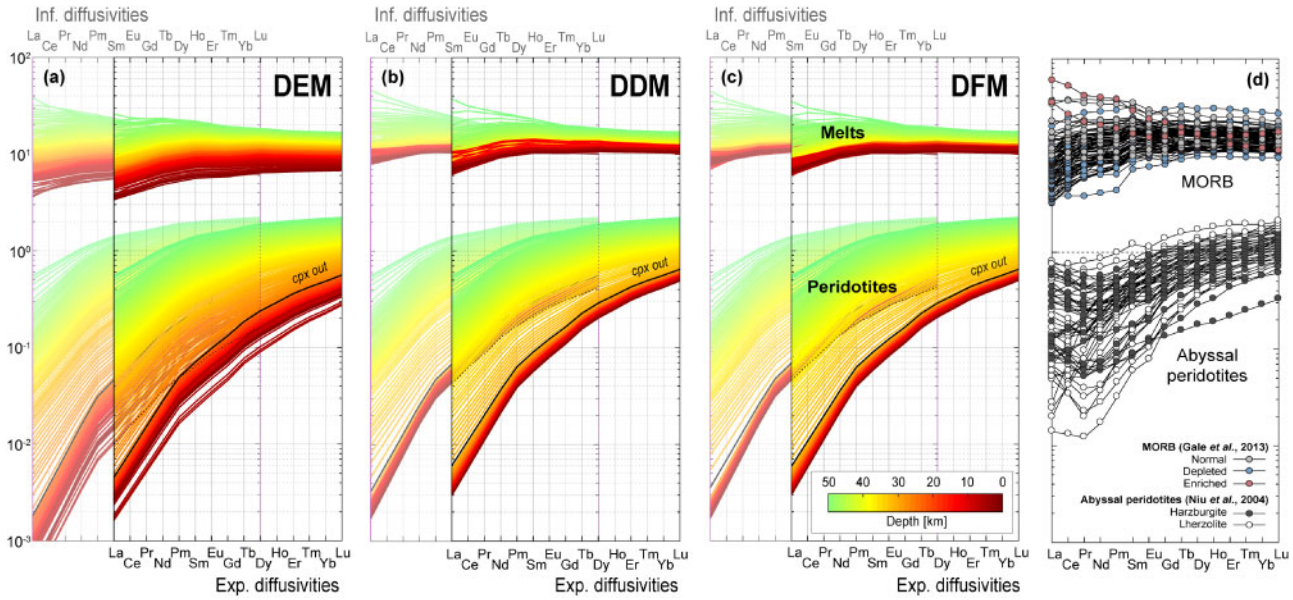

Fig. 12. Comparison between chondrite-normalized REE compositions of peridotites and melts obtained for (a) DEM, (b) DDM, and (c) DFM models using both infinitely fast (left panels) and experimental (right panels) diffusivities of trace elements. Data for Pr, Pm, Tb, Ho, Tm and Lu have been interpolated. Compositions of abyssal peridotites after Niu (2004) and MORB after Gale *et al.* (2013). Chondrite compositions after McDonough & Sun (1995).

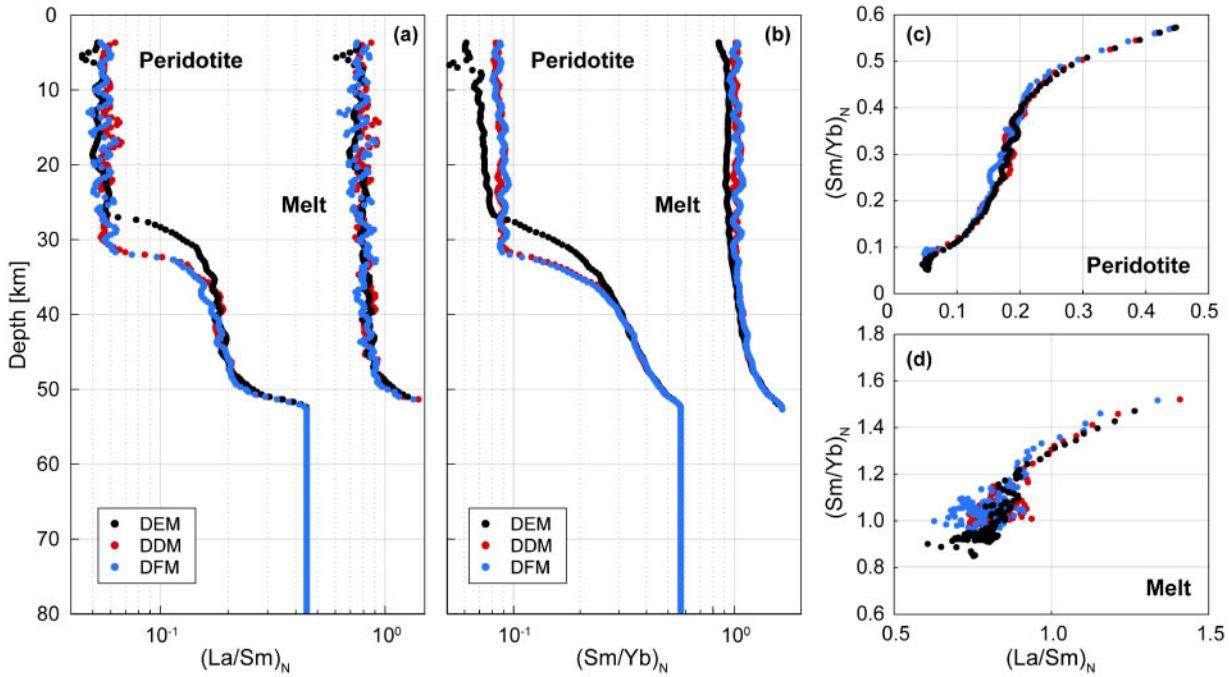

Fig. 13. Evolution with depth of the slope of the (a) LREE [i.e. $(La/Sm)_N$] and (b) HREE [i.e. $(Sm/Yb)_N$] in peridotites and melts for DEM, DDM and DFM models and infinite trace-element diffusivities. (c) $(Sm/Yb)_N$ vs $(La/Sm)_N$ in melts; (d) $(Sm/Yb)_N$ vs $(La/Sm)_N$ in peridotites. Chondrite compositions after McDonough & Sun (1995).

Trace-element systematics. Disequilibrium is expected to alter the trace-element composition of both melts and residual peridodites obtained in equilibrium (Iwamori, 1993; Van Orman *et al.*, 2002*a*). For the sake of clarity, in this section we distinguish between two different 'types' of disequilibrium processes that affect trace element partitioning. The first one relates to the chemical disequilibrium of major elements in the melting model, hereafter referred to as chemical disequilibrium. This type of disequilibrium is the one discussed in the previous sections, which affects the peridotite mineralogy and melt abundance among many other factors. The second type of disequilibrium arises from diffusional re-equilibration of trace elements within

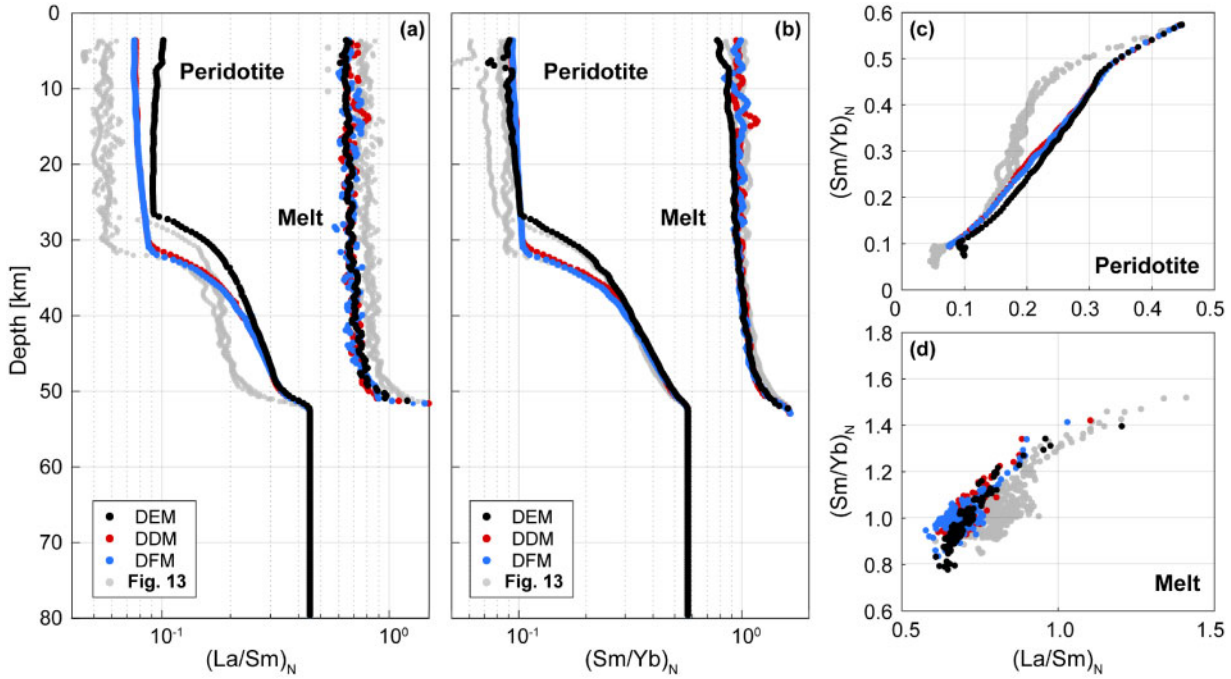

Fig. 14. Evolution with depth of the slope of the (a) LREE and (b) HREE in peridotites and melts for DEM, DDM and DFM models and experimental trace-element diffusivities (see text for details). (c) $(Sm/Yb)_N$ vs $(La/Sm)_N$ in peridotites; (d) $(Sm/Yb)_N$ vs $(La/Sm)_N$ in melts. Grey dots in the background refer to model results shown in Fig. 13 for infinitely fast diffusivities. Chondrite compositions after McDonough & Sun (1995).

mineral grains. Although both types of disequilibrium are ultimately related to diffusion (of major and trace elements, respectively), the latter is referred to as diffusional disequilibrium, as it is solely the result of diffusion and does not affect the equilibrium mineral assemblage.

We first consider the impact of chemical disequilibrium, while assuming instantaneous equilibration (i.e. ultra-fast diffusion) of trace elements within mineral grains. The range of REE patterns in melts are more restricted if some extent of chemical disequilibrium is permitted, with the exception of the very first (and low fraction) melts that exhibit slightly more LREE-enriched patterns (melts in Fig. 12, left panels). In particular, DDM and DFM melts have higher $(Sm/Yb)_N$ at a given depth (above unity, Fig. 13b) and at a given $(La/Sm)_N$ (Fig. 13d) than DEM melts. These differences result from the combined effects of aggregated melt compositions approaching that of near-solidus melts and the more restrictive melt–peridotite chemical interactions, as discussed above. Also, as less melt is extracted in the disequilibrium cases, residual peridotites have (1) higher bulk REE contents (peridotites in Fig. 12b and c) and (2) higher $(Sm/Yb)_N$ at a given depth compared with the equilibrium cases (Fig. 13b). Apart from this, the REE patterns of residual peridotites are similar to those predicted by equilibrium models.

If diffusional disequilibrium is considered in conjunction with chemical equilibrium (i.e. using experimental diffusivities and DEM; black dots in Fig. 14), melts have slightly lower $(La/Sm)_N$ at a given depth (Fig. 14a), but also at a given $(Sm/Yb)_N$ (Fig. 14d) compared with the results with fast equilibration of trace elements (Fig. 13). This difference is more prominent in residual peridotites, which experience significantly less LREE depletion when using experimental trace-element diffusivities (Fig. 14c). Furthermore, LREE become only moderately more depleted than middle REE (MREE) and HREE (Fig. 12a right panel). As far as REE are concerned, experimental diffusivities yield REE compositions comparable with batch melting (Fig. 12a right panel). In contrast, REE compositions obtained using infinite diffusivities approach those of fractional melting models (as they provide strong LREE-to-MREE fractionation, even though DEM is considered here; Fig. 12a left panel).

As discussed above, major-element systematics of abyssal peridotites (e.g. negative $MgO–SiO_2$ correlation) are well accounted for by equilibrium melting models (i.e. DEM). In contrast, their strong LREE depletion in Cpx has been held as evidence for some extent of fractional or near-fractional melting beneath ocean ridges (Johnson *et al.*, 1990), despite the fact that the residual nature of abyssal Cpx is arguable in the absence of detailed petrographic evidence (Seyler *et al.*, 2004). Two main explanations have been proposed to account for this discrepancy between major- and trace-element compositions: on the one hand, a spatial combination of batch and fractional melting (Asimow, 1999); and on the other, the addition of Ol to fractional-melting residues at shallow depths (Niu, 1997, 2004). Alternatively, our results suggest that diffusion-controlled

disequilibrium models in conjunction with DEM can produce melting regimes with residual peridotites that have the major-element characteristics expected from batch melting models, while producing strong LREE depletion, as expected from fractional melting models. We propose an alternative mechanism (e.g. diffusional re-equilibration) to reconcile major- and trace-element compositions of abyssal peridotites and field observations suggesting that extensive re-equilibration does occur between peridotites and melts (e.g. Kelemen *et al.*, 1992; Braun & Kelemen, 2002; Abily & Ceuleneer, 2013; Dygert *et al.*, 2016; Tilhac *et al.*, 2016). This interpretation still requires sufficiently fast diffusional re-equilibration of the REE (e.g. through small grain size and/or long residence time) to reproduce the LREE depletion with experimentally determined diffusivities; microstructural approaches tackling this issue are discussed in 'Model caveats and further developments'. Nonetheless, this conclusion supports the first-order importance of mantle potential temperature during oceanic magmatism (e.g. Dick *et al.*, 1984; Niu & Batiza, 1993) and contrasts with the Ol-addition model evoked above, although the latter hypothesis may be consistent with the strong MREE-to-HREE fractionation observed in certain abyssal peridotites [i.e. very low $(Gd/Yb)_N$]. It is thus reasonable to envisage that both processes probably take place locally, unless such abyssal peridotites with low $(Gd/Yb)_N$ coincidentally experienced higher melting degrees of more fertile lithologies. In any case, an additional process to account for the LREE enrichment of some abyssal peridotites (Bodinier & Godard, 2014) seems unavoidable (e.g. late stage of small-volume melt circulation or fluxed melting involving LREE-enriched fluids). We emphasize that the steady-state model presented here is not expected to reproduce these U-shaped REE patterns, and that a transient model accounting for chromatographic re-equilibration (e.g. Vernières *et al.*, 1997) and/or fractional crystallization of residual melts (e.g. Ozawa, 2001) should be considered instead.

Finally, when diffusional and chemical disequilibrium are combined, melts have even lower $(La/Sm)_N$ at a given $(Sm/Yb)_N$ (Fig. 14d), and slightly more restricted $(Sm/Yb)_N$ values (Fig. 14b). Such melt compositions are reminiscent of MORB compositions (the MREE-to-HREE slope is not as markedly negative; Fig. 12d), and are commonly ascribed to the presence of residual Grt in their source (Kay & Gast, 1973). However, melting is restricted to the stability field of Spl peridotites in these models. We explain this result by the combined effect of slight differences in diffusivities between MREE and HREE in Cpx (Van Orman *et al.*, 2001), the lesser contribution of melt–peridotite interaction, and the greater contribution of near-solidus melts in chemical disequilibrium, which all tend to weaken the MREE-to-HREE depletion. Implications of such disequilibrium processes for interpreting the garnet signature of MORB (as potentially being a 'disequilibrium' signature) can be envisaged (e.g. Grose & Afonso, 2019), but will need to be further assessed by two-dimensional models in combination with U-series disequilibrium, and additional systematic studies of model parameters.

Model caveats and further developments

The current model setup has been designed to mimic mantle upwelling and melting in a setting comparable with the axis of a mid-ocean-ridge in response to an imposed lithospheric extension. Therefore, the chemical signatures described above relate to particular model choices (e.g. single dimension, viscous passive upwelling, thermal profile). Here we envisage four model choices that will need to be revisited if other reactive transports systems are to be studied.

First, the current model considers a linear viscous rheology (i.e. Newtonian), where the viscosity follows a temperature- and pressure-dependent Arrhenius law. Thus, known effects such as the dependence of mantle viscosity on grain size, stress, composition and/or anisotropy have been neglected. Some of these complexities are the focus of several studies, where heterogeneous modes of transport within the asthenosphere have been identified. These range from melt focusing owing to feedbacks between melt–rock reaction and compaction (Aharonov *et al.*, 1995; Spiegelman *et al.*, 2001; Spiegelman & Kelemen, 2003; Liang & Peng, 2010), to fully visco-elasto-plastic rheologies (Connolly & Podladchikov, 2007; Keller *et al.*, 2013; Yarushina & Podladchikov, 2015; Oliveira *et al.*, 2018) or melt infiltration as a consequence of nonlinear porosity waves (Hesse *et al.*, 2011; Liang *et al.*, 2011). As shown by Oliveira *et al.* (2018), our model framework can be readily extended to study general reactive transport processes in combination with visco-elasto-plastic rheologies or other deformation modes [e.g. refertilization processes in the subcontinental lithospheric mantle (Van der Wal & Bodinier, 1996; Griffin *et al.*, 1998; Bodinier *et al.*, 2008); rheological weakening (Farla *et al.*, 2013, among others)].

Second, the thermodynamic model is restricted to dry melting. However, it is generally accepted that 'wet' melting in the deforming mantle is the rule rather than the exception, and that the presence of water in the source can modify not only the chemical compositions of melts and solid residues but also the dynamics of the system. The role of water (and volatiles in general) in mantle melting regimes has been addressed in many previous studies (e.g. Hirth & Kohlstedt, 1996; Asimow & Langmuir, 2003; Grove *et al.*, 2006; Hirschmann, 2006; Keller & Katz, 2016, and references therein). In essence, the main effect of adding water to the source are (1) the lowering of the peridotite solidus, (2) the generation of a low-degree hydrous melting region at depth and (3) the formation of high-flux melt channels owing to reactive-transport feedbacks (Keller *et al.*, 2017). The quantitative interpretation of modelled REE compositions would thus greatly benefit from the inclusion of water, as melt fraction plays a critical role during trace-

element partitioning, and at the current stage, interpretations are partly hampered by the relatively large melt fractions retrieved from the thermodynamic model.

Third, melting is an inherently microscale process. As such, a true description of melting systems far from equilibrium requires a microstructural approach that takes grain geometry, mineral phase distribution and other small-scale features into account. Because an actual non-equilibrium thermodynamic approach adds additional layers of complexity (e.g. Rudge *et al.*, 2011), this study presents a simpler Dynamic Disequilibrium Melting (DDM) model instead. Despite its relative simplicity, we consider that the three coexisting thermodynamic subsystems defined in the current DDM framework provide a valid starting point to hypothesize about the consequences of different possible equilibrium or disequilibirium scenarios, including thermal disequilibrium between liquid and solid residue. Similarly, the disequilibrium partitioning of trace elements between different mineral phases and melts is modelled through a relatively simple grain-scale approach (e.g. spherical grains, absence of coalescence and grain formation, uniform grain size distributions). The extension of both models towards more realistic grain-scale, non-equilibrium thermodynamics approaches is in our agenda (e.g. Grose & Afonso, 2019), but left for future work. However, it is certainly worth devoting some effort to understanding the first-order features of simpler melting models, including varying the degree of re-equilibration of both solid and liquid phases (i.e. other values of characteristic diffusion coefficients) and/or incorporating thermal disequilibrium between solid and liquid phases, before entangling the feedbacks of disequilibrium processes occurring at mineral scale by means of true microstructural approaches.

Finally, our model is particularly well suited to study the impact of mixed sources in the melt generation and transport processes. Our numerical example in 'Model response to a heterogeneous source' consistently predicts several thermal effects consequent to peridotite–pyroxenite melting. For instance, we are able to reproduce the lower solidus temperature of pyroxenites (Morgan, 2001; Pertermann & Hirschmann, 2003; Lambart *et al.*, 2009), because of the internally consistent thermodynamic treatment of melting. Furthermore, our model quantifies the conductive heat exchange between subsolidus peridotites and partially molten pyroxenites, which results in the undercooling of peridotitic mantle, further enhancing the preferential melting of the pyroxenites (Sleep, 1984). For the tested setting, and contrary to the prediction by Brunelli *et al.* (2018), the end of melting region remains unchanged, probably as a consequence of the relatively high extraction rate imposed in the upper part of the domain. Furthermore, and in agreement with Morgan (2001), Sobolev *et al.* (2005) and Lambart (2017), pyroxenites do not fully melt during mantle upwelling in our simulations. Perhaps more interestingly, the interaction between the pyroxenitic melts and peridotites creates a thermally driven chain of processes (explained in detail in 'Model response to a heterogeneous source'), which may be important in unravelling the role of pyroxenites and pyroxenite melts in the generation of basaltic magmas and oceanic crust, and/or when identifying source lithologies involved in melt–peridotite interaction and metasomatism. However, the significance of these processes is still to be investigated in detail. Among many other factors, taking into account the geometry and distribution of the lithological heterogeneities will be particularly important as it may enhance modes of transport that will in turn strongly influence mantle and crustal dynamics (e.g. channelized flow as a consequence of reaction-infiltration instabilities; Aharonov *et al.*, 1995; Spiegelman *et al.*, 2001; Katz & Weatherley, 2012). Further petrological implications of these complexities arising from heterogeneous source melting will be the subject of a companion paper.

CONCLUSIONS

We have presented a conceptual and numerical model to simulate complex thermo-chemical-mechanical processes involved in mantle magmatism. In this model, solid and melt fractions are allowed to evolve in disequilibrium, and to interact thermally, chemically, and mechanically with each other as dictated by coupled energy, mass and momentum conservation equations. The extent of chemical interaction between solid residues and melts is modelled separately for major- and trace-element systematics: major-element chemistry is modelled with a novel Dynamic Disequilibrium Melting model, whereas trace-element exchange is computed with a grain-scale diffusion-controlled disequilibrium model.

The relevance of this integrated approach for interpreting geochemical signatures is demonstrated by analyzing the compositional variability of melts and residual peridotites through simple 1D decompression-melting experiments. The main implications of our findings can be summarized as follows.

1. The main thermo-chemical interactions controlling the compositional variability of melts and residual peridotites during decompression melting are captured by our model. In particular, our results suggest that the major-element systematics of abyssal peridotites can be explained by partial melting alone, provided that melt extraction occurs over a sufficiently wide range of depths and some extent of chemical equilibration is achieved between melts and residues.
2. Disequilibrium plays an important role in the thermo-chemical feedback controlling melt extraction and migration. Its main compositional consequences arise from the smaller melt fraction involved, leading to lowered consumption of latent heat of melting and the prevalence of near-solidus melts on aggregated melt compositions.

3. Chemical disequilibrium results in melt compositions characterized by a negative correlation between Na_2O and FeO for a given T_p, which suggests that caution is required in the geophysical interpretation of regional or global MORB trends. Furthermore, CaO/Al_2O_3 continuously increases after the exhaustion Cpx in disequilibrium, suggesting that this ratio may not be a straightforward proxy of melting degree if disequilibrium is significant.
4. In peridotites, low-volume crystallization of Ol-rich lithologies can be expected when basalts ascend in chemical disequilibrium in the asthenospheric mantle, potentially accounting for the occurrence of Ol gabbros and wehrlite in the deep sections of ophiolites.
5. Fast diffusional re-equilibration of trace elements in conjunction with Dynamic Equilibrium Melting models can reconcile major- and trace-element compositions of abyssal peridotites and field observations, such as dunite channels. This points to extensive interaction (i.e. favouring local equilibrium) between peridotites and melts.
6. The combined effects of slight differences in diffusivities between MREE and HREE in Cpx and lower melt fractions obtained in disequilibrium tend to weaken the MREE-to-HREE depletion resulting from partial melting. Consequently, it could be envisaged that a 'disequilibrium' component may contribute to the garnet signature of MORB even in the absence of garnet in their source.
7. A preliminary model involving melting of a heterogeneous source suggests that the preferential melting of pyroxenites plays an important role in the thermal history recorded by melts and peridotites. Although a thorough quantification of the thermal effects of pyroxenites on mantle melting still requires further work, we demonstrated that our model is particularly well suited to study the petrological and geochemical consequences of such heterogeneous sources.

We acknowledge that the modelling framework discussed in this paper still represents an oversimplification of magmatic process. However, it is general and readily extendable to accommodate numerous processes of geochemical relevance, including melt refertilization, hydrous melting, and/or isotope fractionation. It is also suitable to be incorporated into inversion schemes for melting conditions and source composition. These topics are the focus of forthcoming publications.

ACKNOWLEDGEMENTS

We thank T. Keller, J.-L. Bodinier and P. Asimow for their thorough and constructive reviews. We also thank O. Alard, M. Klöcking, G. Ceuleneer, S. Foley, W. L. Griffin and S. Y. O'Reilly for their insightful remarks at various stages of this work. This is contribution 1510 from the ARC Centre of Excellence for Core to Crust Fluid Systems (www.ccfs.mq.edu.au) and 1394 from the GEMOC Key Centre (www.gemoc.mq.edu.au).

FUNDING

B.O. and J.C.A. acknowledge funding from Macquarie University, ARC Grant DP160103502 and ARC Linkage Grant LP170100233. B.O., J.C.A. and R.T. also acknowledge support from the ARC Centre of Excellence Core to Crust Fluids Systems (CCFS), the Centre for Earth Evolution and Dynamics (CEED) and the European Space Agency via the '3D Earth—A Dynamic Living Planet'.

SUPPLEMENTARY DATA

Supplementary material is available at *Journal of Petrology* online.

APPENDIX A: NUMERICAL IMPLEMENTATION

The numerical strategy used to solve the coupled system of equations heavily relies on our previous studies (Oliveira *et al.*, 2016, 2018). The spatial and temporal discretization of the two-phase reactve transport module is, for instance, identical: a mixed finite-element formulation for the mechanical problem (Oliveira *et al.*, 2018) and a Lagrangian–Eulerian formalism for the energy and chemical transport problem (Oliveira *et al.*, 2016). Three sets of Lagrangian particles are used by the Lagrangian–Eulerian method, one for each advecting field (i.e. different set of particles for the advection of temperature, and solid and liquid phases). The trace-element compositions of both solid and liquid phases are discretized using the same Lagrangian–Eulerian method. In every solid particle, the trace-element concentration distribution within each mineral grain is solved numerically using a fully implicit Crank–Nicolson Finite Element algorithm. For each mineral grain within solid particles a fixed number of radial grid points is maintained throughout the calculation, and phase transformations (i.e. changes in mineral radii) are accommodated by re-scaling. Interpolation of field information between particles and nodes is carried as described by Oliveira *et al.* (2016). We keep control of the density of particles (number of particles per Eulerian cell), by adding or removing particles when needed (Oliveira *et al.*, 2016).

Below we briefly summarize the numerical procedure for a single time step, and provide further details on the implementation of the diffusion-controlled trace-element model.

1. Retrieve initial condition from the previous time step n. This includes velocities $[v_{s,l}]^n$, pressures $[P_{s,l}]^n$, temperature $[T]^n$, major-element chemical

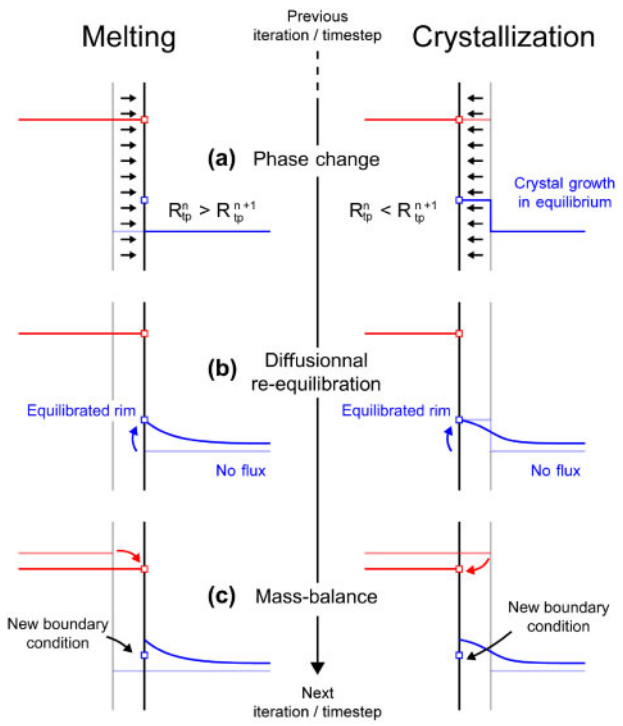

Fig. 15. Three main steps and assumptions for the trace-element mass-transfer computation between mineral grains (blue profiles) and melt (red lines) during melting (left panels) and crystallization (right panels). For a given time step, trace element concentration in melt and mineral grains will in general be in disequilibirum (equilibrium concentrations are marked with squares on the grain boundary). In the phase-change step (a), we assume that the trace-element concentration within the minerals does not change during melting (left, $[R_{tp}]^n > [R_{tp}]^{n+1}$), whereas the outer rims of the minerals are assumed to grow in equilibrium with the surrounding melt in the case of crystallization (right, $[R_{tp}]^n < [R_{tp}]^{n+1}$). During the diffusional re-equilibration step (b), melt–mineral equilibrium is assumed at the grain boundary. Finally, in the mass-balance step (c), the mineral's gain or loss of trace elements is accommodated by the respective concentration loss or gain in the melt. We continue with this iterative procedure (a)–(b)–(c) until the new melt composition reaches equilibrium with every mineral's rim (i.e. $c^e_{tp}(r = R_{tp}) = K^e_{tp} c^e_l$).

composition for each lithology and liquid phase $[c^b_{ss1,s}; c^b_{ss2,s}; c^b_{ss3,s}; c^b_l]^n$, volume fractions of each lithology and liquid phase $[\phi_{ss1,s}; \phi_{ss2,s}; \phi_{ss3,s}; \phi_l]^n$, phase abundances within each subsystem $[\phi_{tp}]^n$ (where $tp = \{\text{ol; cpx; opx; grt; sp; pl}\}$ within each subsystem), physical properties $[\Phi_{s,l}]^n$ (where Φ refers to density, heat capacity, etc.) and mass-transfer rates $[\Gamma]^n$ and $[\Gamma^b]^n$.

2. Assume velocities $[v_{s,l}]^{n+1} = [v_{s,l}]^n$, pressures $[P_{s,l}]^{n+1} = [P_{s,l}]^n$, properties $[\Phi_{s,l}]^{n+1} = [\Phi_{s,l}]^n$, and mass-transfer rates $[\Gamma]^{n+1} = [\Gamma^b]^{n+1} = 0$ to start the non-linear iterations for the coupled Two-Phase Multi-Component Reactive Transport model and the Dynamic Disequilibrium Melting model.
   a. Solve energy equation [equation (17)] assuming the latent heat of phase change from the previous iteration, $\Delta H\Gamma$, and obtain $[T^{n+1}]$.
   b. Solve the mass conservation equations [equations (18), (19), (11)] and the Dynamic Disequilibrium Melting model to obtain major element chemical compositions $[c^b_{ss1,s}; c^b_{ss2,s}; c^b_{ss3,s}; c^b_l]^{n+1}$, volume fractions $[\phi_{ss1,s}; \phi_{ss2,s}; \phi_{ss3,s}; \phi_l]^{n+1}$, mineral phase abundances within subsystems $[\phi_{tp}]^{n+1}$, physical properties $[\Phi_{s,l}]^{n+1}$ and closure terms.
   c. Check convergence in temperature. Go back to (2a) if convergence is not reached.
   d. Solve the mechanical problem [equations (12), (13), (15) and (16)] with the updated set of properties, to obtain $[v_{s,l}]^{n+1}$ and $[P_{s,l}]^{n+1}$.
   e. Check convergence in velocities and update time-step according to Courant number. Go back to (2a) if convergence is not reached.
3. Retrieve $[v_{s,l}]^{n+1}$, $[\phi_{tp}]^{n+1}$ and $[\phi_l]^{n+1}$ and other physical properties from the two-phase multi-component reactive model and the DDM model, including trace-element diffusivities and partition coefficients. Solve grain-size evolution model [equations (23) and (24)] to obtain $[n_{tp}]^{n+1}$ and $[R_{tp}]^{n+1}$. Proceed with the trace-element transport problem as follows.
   a. Re-scale the mesh to accommodate changes in the radii (i.e. $[R_{tp}]^{n+1} \neq [R_{tp}]^n$ owing to phase change). For each mineral grain, a fixed number of radial points is maintained throughout the calculation (non-conforming mesh, higher point density towards the rim).
   b. Prior to the 1D diffusion re-equilibration computation, interpolate $[c^e_{tp}]^{n+1}$ to the new radial mesh. If any point of the new grain lies outside the interval spanned by the previous mesh (i.e. crystallization), that node is assumed to be in equilibrium with the fluid and, as such, $c^e_{tp}(r > R_{tp}) = K^e_{tp} c^e_l$ (Fig. 15a).
   c. Solve the 1D diffusion problem for trace elements [equation (20) with boundary conditions in equations (21) and (22)] and obtain $[c^e_{tp}(r)]^{n+1}$ (Fig. 15b).
   d. Compute the mass-balance [equation (26)] and obtain $[\Gamma^e]^{n+1}$ (Fig. 15c).
   e. Solve the trace-element mass conservation equation for the liquid phase [equation (25)] and obtain $[c^e_l]^{n+1}$.
   f. Update the boundary condition at the boundary of the grains, $[c^e_{tp}]^{n+1}$. Go to step (3b) if convergence of every trace-element concentration at every grain boundaries is not achieved.
4. Check time and go to (1) for the next time step.

A MATLAB implementation of all the above steps is available from the authors upon request.

APPENDIX B: THERMODYNAMIC MODEL

GIBBS FREE-ENERGY MINIMIZATION

Let us consider a system in which pressure, temperature and chemical composition are known. A complete

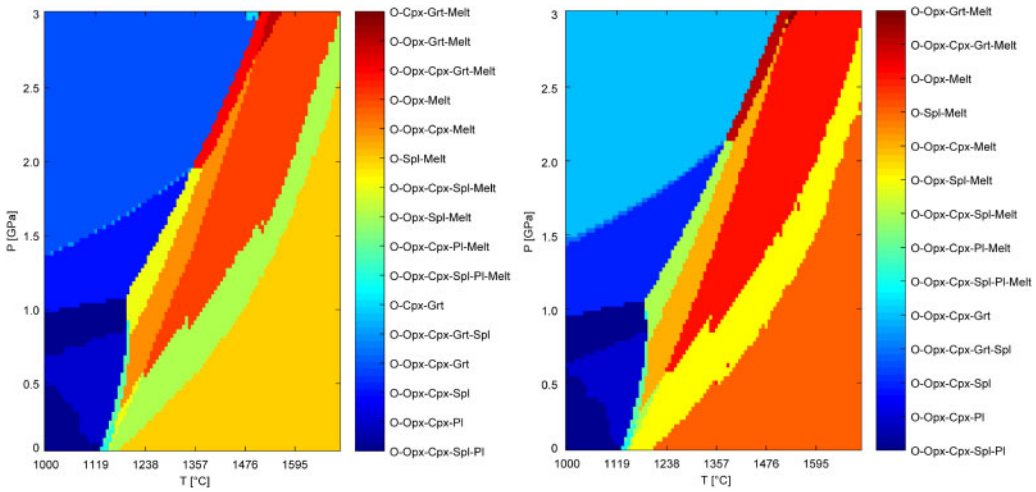

Fig. 16. *P–T* pseudosections for KLB-1 composition (a) without O_2 and (b) with O_2. Phase diagrams are calculated as in fig. 1 of Jennings & Holland (2015).

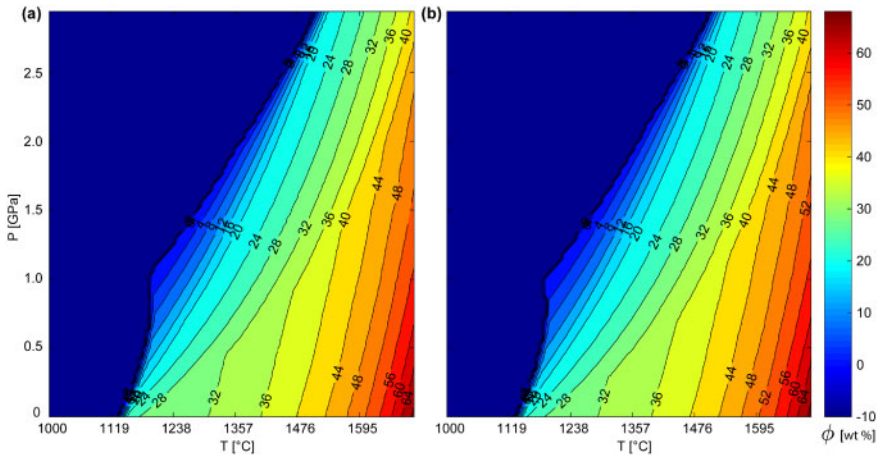

Fig. 17. *P–T* melt abundance (in wt%) for KLB-1 composition (a) without O_2 and (b) with O_2. Phase diagrams are calculated as in fig. 1 of Jennings & Holland (2015).

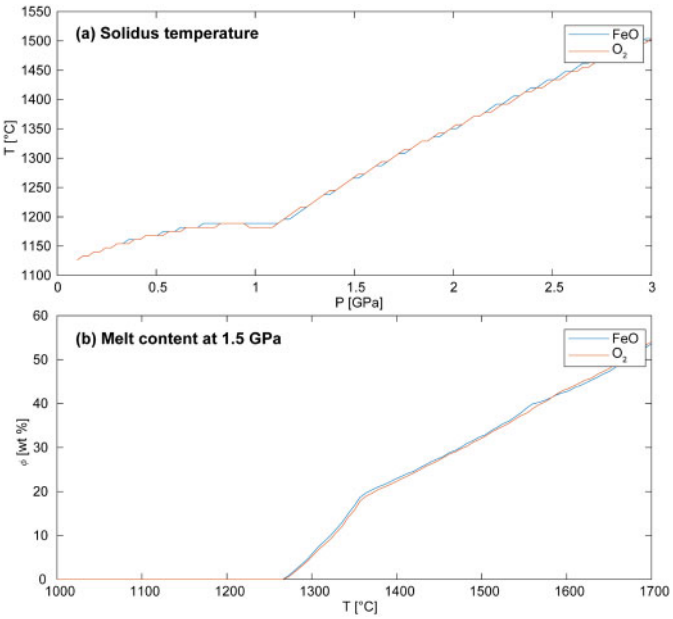

Fig. 18. (a) Solidus pressure, and (b) melt fraction as a function of temperature [computed as in fig. 5 of Jennings & Holland (2015)].

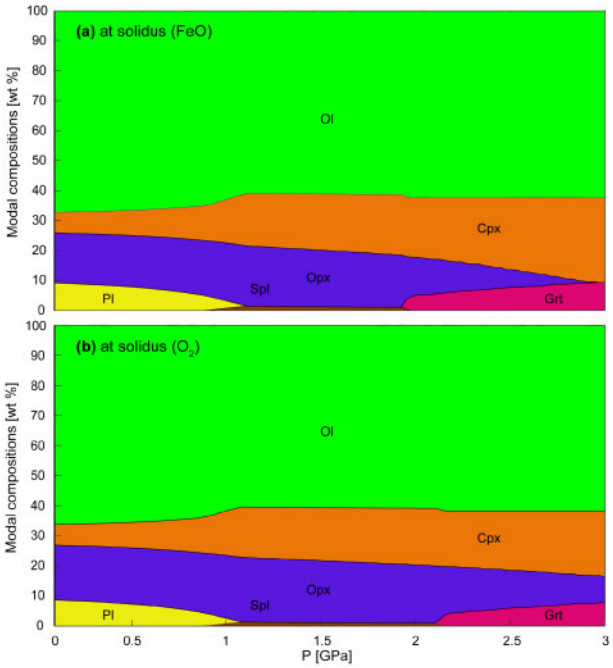

Fig. 19. Modebox diagram at pressures along the solidus (a) without O_2 and (b) with O_2, as in fig. 6 of Jennings & Holland (2015).

description of the equilibrium mineralogical assemblage in terms of physical properties, thermodynamic phase abundances and their individual compositions can be computed by minimizing (locally) the Gibbs free energy of the system, at constant P–T–c^b subject to mass-balance constraints among thermodynamic phases and bulk composition, c^b, as

$$\text{minimize } G_{\text{syst}} = \sum\nolimits_i X_i G_i \tag{27}$$

$$\text{subject to } c^b = A_{bi} X_i$$

$$\text{and } X_i \geq 0$$

where i refers to the thermodynamic phases coexisting in equilibrium, G_i is the molar Gibbs energy of phase i, X_i is the molar amount of phase i, c^b is the composition vector, and A_{bi} is the coefficient matrix containing the equilibrium compositions of each phase i (i.e. amount of b component in the ith thermodynamic phase). The local minimization problem in equation (27) involves finding the amounts and compositions of the thermodynamic phases that minimize the Gibbs free energy of the (local) system for a given temperature, pressure and bulk chemical composition. Once G_i values for all the coexisting thermodynamic phases are known, the

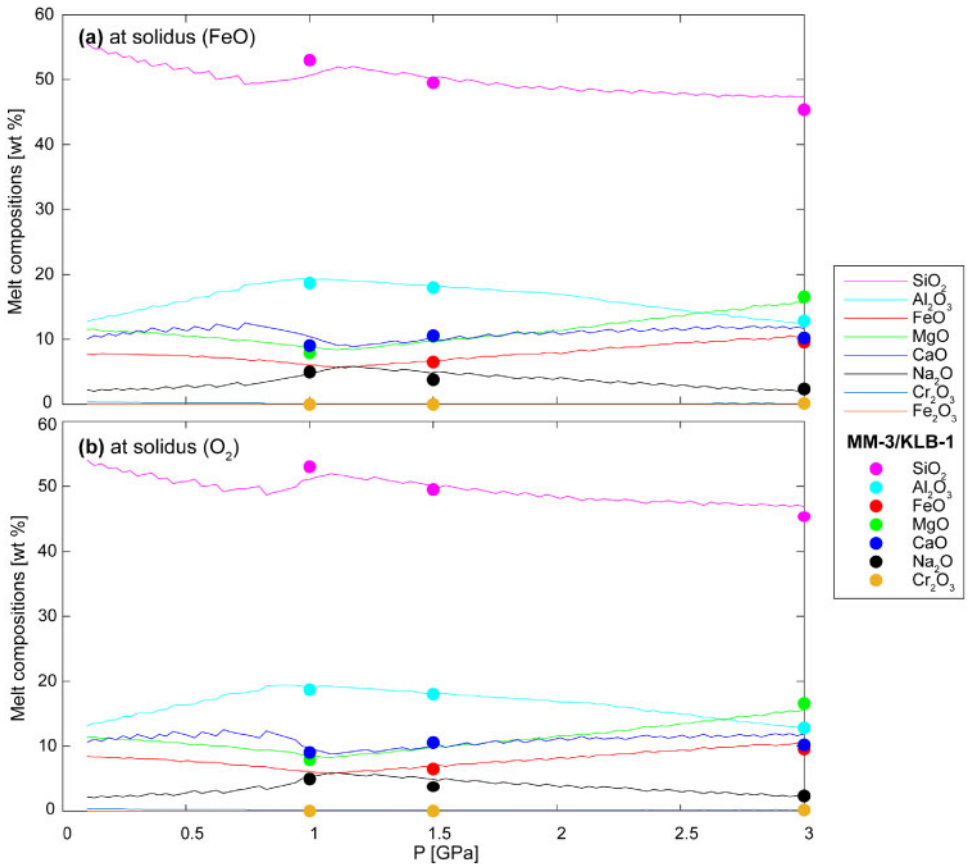

Fig. 20. Calculated major-element composition of melts along the solidus (a) without O_2 and (b) with O_2, as in fig. 8 of Jennings & Holland (2015). Filled circles are compositions at 1 and 1·5 GPa from bulk composition MM-3 (Falloon *et al.*, 2008, and references therein); 3 GPa points from KLB-1 (Davis *et al.*, 2011).

computation of their thermodynamic properties and bulk mass- transfer rates Γ and Γ^b in local equilibrium is straightforward (e.g. Tirone *et al.*, 2009; Oliveira *et al.*, 2018).

THERMODYNAMIC MODEL VALIDATION

Gibbs free-energy minimizations are performed using components of the software Perple_X (Connolly *et al.*, 2009) together with the thermodynamic model and database of Jennings & Holland (2015). The employed Perplex solution model, thermodynamic database, and additional files can be found in the supplementary material for full reproduction of the thermodynamic model. In Figs 16–20 our thermodynamic model is compared with results reported by Jennings & Holland (2015) for KLB-1 composition. We test the effect of neglecting O_2 in the thermodynamic formulation. The bulk composition for KLB-1 is that of Davis *et al.* (2009). The overall agreement between models validates the implementation of our thermodynamic model without O_2.

REFERENCES

Abily, B. & Ceuleneer, G. (2013). The dunitic mantle–crust transition zone in the Oman ophiolite: Residue of melt–rock interaction, cumulates from high-MgO melts, or both? *Geology* **41**, 67–70.

Afonso, J. C. & Zlotnik, S. (2011). The subductability of continental lithosphere: The before and after story. In: Brown, D. & Ryan, P. D. (eds) *Arc–Continent Collision*. Berlin: Springer, pp. 53–86.

Aharonov, E., Whitehead, J. A., Kelemen, P. B. & Spiegelman, M. (1995). Channeling instability of upwelling melt in the mantle. *Journal of Geophysical Research: Solid Earth* **100**, 20433–20450.

Asimow, P. D. (1999). A model that reconciles major- and trace-element data from abyssal peridotites. *Earth and Planetary Science Letters* **169**, 303–319.

Asimow, P. D. (2001). Calculation of peridotite partial melting from thermodynamic models of minerals and melts, IV. Adiabatic decompression and the composition and mean properties of mid-ocean ridge basalts. *Journal of Petrology* **42**, 963–998.

Asimow, P. D. (2002). Steady-state mantle–melt interactions in one dimension: II. Thermal interactions and irreversible terms. *Journal of Petrology* **43**, 1707–1724.

Asimow, P. D. & Langmuir, C. H. (2003). The importance of water to oceanic mantle melting regimes. *Nature* **421**, 815–820.

Asimow, P. D. & Stolper, E. M. (1999). Steady-state mantle–melt interactions in one dimension: I. Equilibrium transport and melt focusing. *Journal of Petrology* **40**, 475–494.

Austin, N. J. & Evans, B. (2007). Paleowattmeters: A scaling relation for dynamically recrystallized grain size. *Geology* **35**, 343–346.

Baker, M. B., Hirschmann, M. M., Ghiorso, M. S. & Stolper, E. M. (1995). Compositions of near-solidus peridotite melts from experiments and thermodynamic calculations. *Nature* **375**, 308.

Bercovici, D. & Ricard, Y. (2003). Energetics of a two-phase model of lithospheric damage, shear localization and plate-boundary formation. *Geophysical Journal International* **152**, 581–596.

Bercovici, D., Ricard, Y. & Schubert, G. (2001). A two-phase model for compaction and damage: 1. General Theory. *Journal of Geophysical Research: Solid Earth* **106**, 8887–8906.

Blundy, J. D., Falloon, T. J., Wood, B. J. & Dalton, J. A. (1995). Sodium partitioning between clinopyroxene and silicate melts. *Journal of Geophysical Research: Solid Earth* **100**, 15501–15515.

Bodinier, J.-L. & Godard, M. (2014). The Mantle and Core. Treatise on Geochemistry. Orogenic, ophiolitic, and abyssal peridotites. In: Holland, H.D., Turekian, K. K. (eds) *Treatise on Geochemistry*, Vol. **3**, 2nd edn. Elsevier, pp. 103–167.

Bodinier, J.-L., Garrido, C. J., Chanefo, I., Bruguier, O. & Gervilla, F. (2008). Origin of pyroxenite–peridotite veined mantle by refertilization reactions: evidence from the Ronda peridotite (Southern Spain). *Journal of Petrology* **49**, 999–1025.

Bodinier, J. L., Godard, M., Holland, H. D. & Turekian, K. K. (2014). *Treatise on Geochemistry, Vol. 2*. Oxford: Elsevier Science.

Braun, M. G. & Kelemen, P. B. (2002). Dunite distribution in the Oman ophiolite: implications for melt flux through porous dunite conduits. *Geochemistry, Geophysics, Geosystems* **3**, 1–21.

Brown, E. L. & Lesher, C. E. (2016). REEBOX PRO: A forward model simulating melting of thermally and lithologically variable upwelling mantle. *Geochemistry, Geophysics, Geosystems* **17**, 3929–3968.

Brunelli, D., Cipriani, A. & Bonatti, E. (2018). Thermal effects of pyroxenites on mantle melting below mid-ocean ridges. *Nature Geoscience* **11**, 520.

Chakraborty, S. & Ganguly, J. (1992). Cation diffusion in aluminosilicate garnets: experimental determination in spessartine–almandine diffusion couples, evaluation of effective binary diffusion coefficients, and applications. *Contributions to Mineralogy and petrology* **111**, 74–86.

Cherniak, D. J. & Watson, E. (1994). A study of strontium diffusion in plagioclase using Rutherford backscattering spectroscopy. Geochimica Et Cosmochimica Acta **58**, 5179–5190.

Cherniak, D. J. & Liang, Y. (2007). Rare earth element diffusion in natural enstatite. *Geochimica Et Cosmochimica Acta* **71**, 1324–1340.

Cherniak, D. J. (2003). REE diffusion in feldspar. *Chemical Geology* **193**, 25–41.

Cherniak, D. J. (2010). REE diffusion in olivine. *American Mineralogist* **95**, 362–368.

Clauser, C. & Huenges, E. (1995). Thermal conductivity of rocks and minerals. In: Ahrens, T.~J., Clauser, C. & Huenges, E. (eds) *Rock physics and phase relations: a handbook of physical constants*. Wiley Online Library. Washington: American Geophysical Union **3**, 105–126.

Connolly, J. A. D. & Podladchikov, Y. Y. (2007). Decompaction weakening and channeling instability in ductile porous media: Implications for asthenospheric melt segregation. *Journal of Geophysical Research: Solid Earth* **112**, B10205.

Connolly, J. A. D., Schmidt, M. W., Solferino, G. & Bagdassarov, N. (2009). Permeability of asthenospheric mantle and melt extraction rates at mid-ocean ridges. *Nature* **462**, 209.

Davis, F. A., Tangeman, J. A., Tenner, T. J. & Hirschmann, M. M. (2009). The composition of KLB-1 peridotite. *American Mineralogist* **94**, 176–180.

Davis, F. A., Hirschmann, M. M. & Humayun, M. (2011). The composition of the incipient partial melt of garnet peridotite at 3 GPa and the origin of OIB. *Earth and Planetary Science Letters* **308**, 380–390.

De Groot, S. R. & Mazur, P. (2013). *Non-equilibrium thermodynamics*. Courier Corporation.

Dick, H. J. B. & Zhou, H. (2015). Ocean rises are products of variable mantle composition, temperature and focused melting. *Nature Geoscience* **8**, 68.

Dick, H. J. B., Fisher, R. L. & Bryan, W. B. (1984). Mineralogic variability of the uppermost mantle along mid-ocean ridges. *Earth and Planetary Science Letters* **69**, 88–106.

Dygert, N., Liang, Y. & Kelemen, P. B. (2016). Formation of plagioclase lherzolite and associated dunite–harzburgite–lherzolite sequences by multiple episodes of melt percolation and melt–rock reaction: an example from the Trinity Ophiolite, California, USA. *Journal of Petrology* **57**, 815–838.

Falloon, T. J., Green, D. H., Danyushevsky, L. V & McNeill, A. W. (2008). The composition of near-solidus partial melts of fertile peridotite at 1 and 1·5 GPa: implications for the petrogenesis of MORB. *Journal of Petrology* **49**, 591–613.

Farla, R. J. M., Karato, S. & Cai, Z. (2013). Role of orthopyroxene in rheological weakening of the lithosphere via dynamic recrystallization. *Proceedings of the National Academy of Sciences of the USA* **110**, 16355–16360.

Faul, U. H. (2001). Melt retention and segregation beneath mid-ocean ridges. *Nature* **410**, 920.

Gale, A., Laubier, M., Escrig, S. & Langmuir, C. H. (2013). Constraints on melting processes and plume–ridge interaction from comprehensive study of the FAMOUS and North Famous segments, Mid-Atlantic Ridge. *Earth and Planetary Science Letters* **365**, 209–220.

Ganguly, J., Cheng, W. & Chakraborty, S. (1998). Cation diffusion in aluminosilicate garnets: experimental determination in pyrope–almandine diffusion couples. *Contributions to Mineralogy and Petrology* **131**, 171–180.

Gast, P. W. (1968). Trace element fractionation and the origin of tholeiitic and alkaline magma types. *Geochimica et Cosmochimica Acta* **32**, 1057–1086.

George, A. M. & Stebbins, J. F. (1996). Dynamics of Na in sodium aluminosilicate glasses and liquids. *Physics and Chemistry of Minerals* **23**, 526–534.

Griffin, W. L., Andi, Z., O'Reilly, S. Y. & Ryan, C. G. (1998). Phanerozoic evolution of the lithosphere beneath the Sino-Korean craton. In: Flower, M. F. J., Chung, S. L., Lo, C. H. & Lee, T. Y. (eds) *Mantle dynamics and plate interactions in East Asia.* Wiley Online Library **27**, 107–126.

Grose, C. J. & Afonso, J. C. (2019). Chemical disequilibria, lithospheric thickness, and the source of ocean island basalts. *Journal of Petrology* **60**, 755–790.

Grove, T. L., Chatterjee, N., Parman, S. W. & Médard, E. (2006). The influence of H_2O on mantle wedge melting. *Earth and Planetary Science Letters* **249**, 74–89.

Herzberg, C. (2004). Partial crystallization of mid-ocean ridge basalts in the crust and mantle. *Journal of Petrology* **45**, 2389–2405.

Hesse, M. A., Schiemenz, A. R., Liang, Y. & Parmentier, E. M. (2011). Compaction–dissolution waves in an upwelling mantle column. *Geophysical Journal International* **187**, 1057–1075.

Hirschmann, M. M. (2006). Water, melting, and the deep Earth H_2O cycle. *Annual Review of Earth and Planetary Sciences* **34**, 629–653.

Hirschmann, M. M., Baker, M. B. & Stolper, E. M. (1998). The effect of alkalis on the silica content of mantle-derived melts. *Geochimica et Cosmochimica Acta* **62**, 883–902.

Hirschmann, M. M., Ghiorso, M. S. & Stolper, M. (1999). Calculation of peridotite partial melting from thermodynamic models of minerals and melts. II. Isobaric variations in melts near the solidus and owing to variable source composition. *Journal of Petrology* **40**, 297–313.

Hirth, G. & Kohlstedt, D. L. (1996). Water in the oceanic upper mantle: implications for rheology, melt extraction and the evolution of the lithosphere. *Earth and Planetary Science Letters* **144**, 93–108.

Hirth, G. & Kohlstedt, D. L. (2003). Rheology of the upper mantle and the mantle wedge: a view from the experimentalists. In: Eiler, J. (ed.) *American Geophysical Union, Geophysical Monographs* **138**, 83–105.

Iwamori, H. (1993). Dynamic disequilibrium melting model with porous flow and diffusion-controlled chemical equilibration. *Earth and Planetary Science Letters* **114**, 301–313.

Iwamori, H., McKenzie, D. & Takahashi, E. (1995). Melt generation by isentropic mantle upwelling. *Earth and Planetary Science Letters* **134**, 253–266.

Jennings, E. S. & Holland, T. J. B. (2015). A simple thermodynamic model for melting of peridotite in the system NCFMASOCr. *Journal of Petrology* **56**, 869–892.

Johnson, K. T. M. (1998). Experimental determination of partition coefficients for rare earth and high-field-strength elements between clinopyroxene, garnet, and basaltic melt at high pressures. *Contributions to Mineralogy and Petrology* **133**, 60–68.

Johnson, K. T. M., Dick, H. J. B. & Shimizu, N. (1990). Melting in the oceanic upper mantle: an ion microprobe study of diopsides in abyssal peridotites. *Journal of Geophysical Research: Solid Earth* **95**, 2661–2678.

Katz, R. F. (2008). Magma dynamics with the enthalpy method: Benchmark solutions and magmatic focusing at mid-ocean ridges. *Journal of Petrology* **49**, 2099–2121.

Katz, R. F. & Weatherley, S. M. (2012). Consequences of mantle heterogeneity for melt extraction at mid-ocean ridges. *Earth and Planetary Science Letters* **335**, 226–237.

Kay, R. W. & Gast, P. W. (1973). The rare earth content and origin of alkali-rich basalts. *Journal of Geology* **81**, 653–682.

Kelemen, P. B., Dick, H. J. B. & Quick, J. E. (1992). Formation of harzburgite by pervasive melt/rock reaction in the upper mantle. *Nature* **358**, 635.

Kelemen, P. B., Hanghøj, K. & Greene, A. R. (2014). One view of the geochemistry of subduction-related magmatic arcs, with an emphasis on primitive andesite and lower crust. In: Holland, H. D. & Turekian, K. K. (eds) *Treatise on Geochemistry*, 3, 659.

Keller, T. & Katz, R. F. (2016). The role of volatiles in reactive melt transport in the asthenosphere. *Journal of Petrology* **57**, 1073–1108.

Keller, T. & Suckale, J. (2019). A continuum model of multi-phase reactive transport in igneous systems. *Geophysical Journal International* **219**, 185–222.

Keller, T., May, D. A. & Kaus, B. J. P. (2013). Numerical modelling of magma dynamics coupled to tectonic deformation of lithosphere and crust. *Geophysical Journal International* **195**, 1406–1442.

Keller, T., Katz, R. F. & Hirschmann, M. M. (2017). Volatiles beneath mid-ocean ridges: Deep melting, channelised transport, focusing, and metasomatism. *Earth and Planetary Science Letters* **464**, 55–68.

Kinzler, R. J. & Grove, T. L. (1992). Primary magmas of mid-ocean ridge basalts 1. Experiments and methods. *Journal of Geophysical Research: Solid Earth* **97**, 6885–6906.

Klein, E. M. & Langmuir, C. H. (1987). Global correlations of ocean ridge basalt chemistry with axial depth and crustal thickness. *Journal of Geophysical Research: Solid Earth* **92**, 8089–8115.

Klein, E. M. & Langmuir, C. H. (1989). Local versus global variations in ocean ridge basalt composition: A reply. *Journal of Geophysical Research: Solid Earth* **94**, 4241–4252.

Klemme, S., Blundy, J. D. & Wood, B. J. (2002). Experimental constraints on major and trace element partitioning during partial melting of eclogite. *Geochimica et Cosmochimica Acta* **66**, 3109–3123.

Lambart, S. (2017). No direct contribution of recycled crust in Icelandic basalts. *Geochemical Perspectives Letters* **4**, 7–12.

Lambart, S., Laporte, D. & Schiano, P. (2009). An experimental study of pyroxenite partial melts at 1 and 1·5 GPa: Implications for the major-element composition of mid-ocean ridge basalts. *Earth and Planetary Science Letters* **288**, 335–347.

Lambart, S., Baker, M. B. & Stolper, E. M. (2016). The role of pyroxenite in basalt genesis: Melt-PX, a melting parameterization for mantle pyroxenites between 0·9 and 5 GPa. *Journal of Geophysical Research: Solid Earth* **121**, 5708–5735.

Langmuir, C. H., Klein, E. M. & Plank, T. (1992). Petrological systematics of mid-ocean ridge basalts: Constraints on melt generation beneath ocean ridges. In: Morgan, J. P., Blackman, D. K. & Sinton, J. M. (eds) *Mantle flow and melt generation at mid-ocean ridges*. Wiley Online Library **71**, 183–280.

Laubier, M., Grove, T. L. & Langmuir, C. H. (2014). Trace element mineral/melt partitioning for basaltic and basaltic andesitic melts: an experimental and laser ICP-MS study with application to the oxidation state of mantle source regions. *Earth and Planetary Science Letters* **392**, 265–278.

Lebon, G., Jou, D. & Casas-Vázquez, J. (2008). *Understanding non-equilibrium thermodynamics*. Berlin: Springer.

Liang, Y. & Peng, Q. (2010). Non-modal melting in an upwelling mantle column: Steady-state models with applications to REE depletion in abyssal peridotites and the dynamics of melt migration in the mantle. *Geochimica et Cosmochimica Acta* **74**, 321–339.

Liang, Y., Schiemenz, A., Hesse, M. A. & Parmentier, E. M. (2011). Waves, channels, and the preservation of chemical heterogeneities during melt migration in the mantle. *Geophysical Research Letters* **38**, L20308.

Lundstrom, C. C. (2003). Uranium-series disequilibria in mid-ocean ridge basalts: observations and models of basalt genesis. In: *Mineralogical Society of America and Geochemical Society, Reviews in Mineralogy and Geochemistry* **52**, 175–214.

McDonough, W. F. & Sun, S.-S. (1995). The composition of the Earth. *Chemical Geology* **120**, 223–253.

McKenzie, D. (1984). The generation and compaction of partially molten rock. *Journal of Computational Physics* **25**, 713–765.

McKenzie, D. (1985). The extraction of magma from the crust and mantle. *Earth and Planetary Science Letters* **74**, 81–91.

Morgan, J. P. (2001). Thermodynamics of pressure release melting of a veined plum pudding mantle. *Geochemistry, Geophysics, Geosystems* **2**, 2000GC000049.

Morse, S. A. (1980). *Basalts and phase diagrams: an introduction to the quantitative use of phase diagrams in igneous petrology*. Berlin: Springer.

Niu, Y. (1997). Mantle melting and melt extraction processes beneath ocean ridges: evidence from abyssal peridotites. *Journal of Petrology* **38**, 1047–1074.

Niu, Y. (2004). Bulk-rock major and trace element compositions of abyssal peridotites: implications for mantle melting, melt extraction and post-melting processes beneath mid-ocean ridges. *Journal of Petrology* **45**, 2423–2458.

Niu, Y. & Batiza, R. (1993). Chemical variation trends at fast and slow spreading mid-ocean ridges. *Journal of Geophysical Research: Solid Earth* **98**, 7887–7902.

Niu, Y. & Hekinian, R. (1997). Spreading-rate dependence of the extent of mantle melting beneath ocean ridges. *Nature* **385**, 326.

O'Hara, M. J. (1968). The bearing of phase equilibria studies in synthetic and natural systems on the origin and evolution of basic and ultrabasic rocks. *Earth-Science Reviews* **4**, 69–133.

Oliveira, B., Afonso, J. C. & Zlotnik, S. (2016). A Lagrangian–Eulerian finite element algorithm for advection–diffusion–reaction problems with phase change. *Computer Methods in Applied Mechanics and Engineering* **300**, 375–401.

Oliveira, B., Afonso, J. C., Zlotnik, S. & Diez, P. (2018). Numerical modelling of multiphase multicomponent reactive transport in the Earth's interior. *Geophysical Journal International* **212**, 345–388.

Ozawa, K. (2001). Mass balance equations for open magmatic systems: Trace element behavior and its application to open system melting in the upper mantle. *Journal of Geophysical Research: Solid Earth* **106**, 13407–13434.

Pertermann, M. & Hirschmann, M. M. (2003). Partial melting experiments on a MORB-like pyroxenite between 2 and 3 GPa: Constraints on the presence of pyroxenite in basalt source regions from solidus location and melting rate. *Journal of Geophysical Research: Solid Earth* **108**, 2125.

Piccardo, G. B. & Guarnieri, L. (2010). The Monte Maggiore peridotite (Corsica, France): a case study of mantle evolution in the Ligurian Tethys. In: Coltorti, M., Downes, H., Grégoire, M., O'Reilly, S.Y. (eds) Petrological Evolution of the European Lithospheric Mantle. *Geological Society, London, Special Publications* **337**, 7–45.

Python, M. & Ceuleneer, G. (2003). Nature and distribution of dykes and related melt migration structures in the mantle section of the Oman ophiolite. *Geochemistry, Geophysics, Geosystems* **4**, 8612.

Qin, Z. (1992). Disequilibrium partial melting model and its implications for trace element fractionations during mantle melting. *Earth and Planetary Science Letters* **112**, 75–90.

Ribe, N. M. (1985). The generation and composition of partial melts in the earth's mantle. *Earth and Planetary Science Letters* **73**, 361–376.

Ricard, Y. & Bercovici, D. (2009). A continuum theory of grain size evolution and damage. *Journal of Geophysical Research: Solid Earth* **114**, B01204.

Richter, F. M. & McKenzie, D. (1984). Dynamical models or melt segregation from a deformable matrix. *Journal of Geology* **92**, 729–740.

Riley, G. N., Jr& Kohlstedt, D. L. (1991). Kinetics of melt migration in upper mantle-type rocks. *Earth and Planetary Science Letters* **105**, 500–521.

Robinson, J. A. C., Wood, B. J. & Blundy, J. D. (1998). The beginning of melting of fertile and depleted peridotite at 1·5 GPa. *Earth and Planetary Science Letters* **155**, 97–111.

Rudge, J. F., Bercovici, D. & Spiegelman, M. (2011). Disequilibrium melting of a two phase multicomponent mantle. *Geophysical Journal International* **184**, 699–718.

Schmeling, H., Marquart, G. & Grebe, M. (2017). A porous flow approach to model thermal non-equilibrium applicable to melt migration. *Geophysical Journal International* **212**, 119–138.

Seyler, M., Lorand, J.-P., Toplis, M. J. & Godard, G. (2004). Asthenospheric metasomatism beneath the mid-ocean ridge: Evidence from depleted abyssal peridotites. *Geology* **32**, 301–304.

Shaw, D. M. (1970). Trace element fractionation during anatexis. *Geochimica et Cosmochimica Acta* **34**, 237–243.

Sleep, N. H. (1984). Tapping of magmas from ubiquitous mantle heterogeneities: an alternative to mantle plumes? *Journal of Geophysical Research: Solid Earth* **89**, 10029–10041.

Sobolev, A. V, Hofmann, A. W., Sobolev, S. V & Nikogosian, I. K. (2005). An olivine-free mantle source of Hawaiian shield basalts. *Nature* **434**, 590.

Spiegelman, M. (1993). Flow in deformable porous media. Part 1 Simple analysis. *Journal of Fluid Mechanics* **247**, 17–38.

Spiegelman, M. & Kelemen, P. B. (2003). Extreme chemical variability as a consequence of channelized melt transport. *Geochemistry, Geophysics, Geosystems* **4**, 1055.

Spiegelman, M. & McKenzie, D. (1987). Simple 2-D models for melt extraction at mid-ocean ridges and island arcs. *Earth and Planetary Science Letters* **83**, 137–152.

Spiegelman, M., Kelemen, P. B. & Aharonov, E. (2001). Causes and consequences of flow organization during melt transport: The reaction infiltration instability in compactible media. *Journal of Geophysical Research: Solid Earth* **106**, 2061–2077.

Šrámek, O., Ricard, Y. & Bercovici, D. (2007). Simultaneous melting and compaction in deformable two-phase media. *Geophysical Journal International* **168**, 964–982.

Stolper, E. (1980). A phase diagram for mid-ocean ridge basalts: preliminary results and implications for petrogenesis. *Contributions to Mineralogy and Petrology* **74**, 13–27.

Streckeisen, A. (1976). To each plutonic rock its proper name. *Earth-Science Reviews* **12**, 1–33.

Sun, C. & Liang, Y. (2014). An assessment of subsolidus re-equilibration on REE distribution among mantle minerals olivine, orthopyroxene, clinopyroxene, and garnet in peridotites. *Chemical Geology* **372**, 80–91.

Tilhac, R., Ceuleneer, G., Griffin, W. L., O'Reilly, S. Y., Pearson, N. J., Benoit, M., Henry, H., Girardeau, J. & Grégoire, M. (2016). Primitive arc magmatism and delamination: petrology and geochemistry of pyroxenites from the Cabo Ortegal complex, Spain. *Journal of Petrology* **57**, 1921–1954.

Tirone, M. (2018). Petrological Geodynamics of Mantle Melting II. AlphaMELTS+ Multiphase Flow: Dynamic Fractional Melting. *Frontiers in Earth Science* **6**, 18.

Tirone, M. & Sessing, J. (2017). Petrological geodynamics of mantle melting I. AlphaMELTS+ multiphase flow: Dynamic equilibrium melting, method and results. *Frontiers in Earth Science* **5**, 81.

Tirone, M., Ganguly, J. & Morgan, J. P. (2009). Modeling petrological geodynamics in the Earth's mantle. *Geochemistry, Geophysics, Geosystems* **10**.

Turner, A. J., Katz, R. F. & Behn, M. D. (2015). Grain-size dynamics beneath mid-ocean ridges: Implications for permeability and melt extraction. *Geochemistry, Geophysics, Geosystems* **16**, 925–946.

Van der Wal, D. & Bodinier, J.-L. (1996). Origin of the recrystallisation front in the Ronda peridotite by km-scale pervasive porous melt flow. *Contributions to Mineralogy and Petrology* **122**, 387–405.

Van Orman, J. A., Grove, T. L. & Shimizu, N. (2001). Rare earth element diffusion in diopside: influence of temperature, pressure, and ionic radius, and an elastic model for diffusion in silicates. *Contributions to Mineralogy and Petrology* **141**, 687–703.

Van Orman, J. A., Grove, T. L. & Shimizu, N. (2002a). Diffusive fractionation of trace elements during production and transport of melt in Earth's upper mantle. *Earth and Planetary Science Letters* **198**, 93–112.

Van Orman, J. A., Grove, T. L., Shimizu, N. & Layne, G. D. (2002b). Rare earth element diffusion in a natural pyrope single crystal at 2·8 GPa. *Contributions to Mineralogy and Petrology* **142**, 416–424.

Van Orman, J. A., Saal, A. E., Bourdon, B. & Hauri, E. H. (2006). Diffusive fractionation of U-series radionuclides during mantle melting and shallow-level melt–cumulate interaction. *Geochimica et Cosmochimica Acta* **70**, 4797–4812.

Vernières, J., Godard, M. & Bodinier, J.-L. (1997). A plate model for the simulation of trace element fractionation during partial melting and magma transport in the Earth's upper mantle. *Journal of Geophysical Research: Solid Earth* **102**, 24771–24784.

von Bargen, N. & Waff, H. S. (1986). Permeabilities, interfacial areas and curvatures of partially molten systems: results of numerical computations of equilibrium microstructures. *Journal of Geophysical Research: Solid Earth* **91**, 9261–9276.

Waff, H. S. & Bulau, J. R. (1979). Equilibrium fluid distribution in an ultramafic partial melt under hydrostatic stress conditions. *Journal of Geophysical Research: Solid Earth* **84**, 6109–6114.

Warren, J. M. (2016). Global variations in abyssal peridotite compositions. *Lithos* **248**, 193–219.

Wasylenki, L. E., Baker, M. B., Kent, A. J. R. & Stolper, E. M. (2003). Near-solidus melting of the shallow upper mantle: partial melting experiments on depleted peridotite. *Journal of Petrology* **44**, 1163–1191.

Workman, R. K. & Hart, S. R. (2005). Major and trace element composition of the depleted MORB mantle (DMM). *Earth and Planetary Science Letters* **231**, 53–72.

Yarushina, V. M. & Podladchikov, Y. Y. (2015). (De) compaction of porous viscoelastoplastic media: Model formulation. *Journal of Geophysical Research: Solid Earth* **120**, 4146–4170.